On numerical instabilities of Godunov-type schemes for strong shocks

CrossMark

Wenjia Xie [a],[*], Wei Li [b], Hua Li [a], Zhengyu Tian [a], Sha Pan [a]

[a] College of Aerospace Science and Engineering, National University of Defense Technology, Hunan 410073, China
[b] Computational Aerodynamics Research Institute, China Aerodynamics Research and Development Center, Sichuan, China

A R T I C L E   I N F O

A B S T R A C T

It is well known that low diffusion Riemann solvers with minimal smearing on contact and shear waves are vulnerable to shock instability problems, including the carbuncle phenomenon. In the present study, we concentrate on exploring where the instability grows out and how the dissipation inherent in Riemann solvers affects the unstable behaviors. With the help of numerical experiments and a linearized analysis method, it has been found that the shock instability is strongly related to the unstable modes of intermediate states inside the shock structure. The consistency of mass flux across the normal shock is needed for a Riemann solver to capture strong shocks stably. The famous carbuncle phenomenon is interpreted as the consequence of the inconsistency of mass flux across the normal shock for a low diffusion Riemann solver. Based on the results of numerical experiments and the linearized analysis, a robust Godunov-type scheme with a simple cure for the shock instability is suggested. With only the dissipation corresponding to shear waves introduced in the vicinity of strong shocks, the instability problem is circumvented. Numerical results of several carefully chosen strong shock wave problems are investigated to demonstrate the robustness of the proposed scheme.

© 2017 Elsevier Inc. All rights reserved.

1. Introduction

In the last decades, great progress has been made in computational fluid dynamics. However, there are still challenging issues that need to be addressed with caution, especially in hypersonic flows. One of them is the accurate prediction of hypersonic heating which relies heavily on the performance of shock-capturing schemes used in a finite-volume Euler/Navier–Stokes code. Approximate Riemann solvers are popular shock-capturing methods for hypersonic flow computations. Not only should a desirable Riemann solver capture all kinds of discontinuities accurately and sharply, but it also should own a high level of robustness against the shock anomalies, including the carbuncle phenomenon. However, it is unfortunate that the carbuncle phenomenon is usually triggered easily by low diffusion Riemann solvers which are designed to capture contact and shear discontinuities with minimal smearing [1]. Since the shock anomalies, in particular, the carbuncle phenomenon, ruin all efforts to resolve grid-aligned shock waves, a large amount of research has been conducted to understand and cure this instability problem.

Quirk [2] concerns the shock instability based on a simplified case: the odd–even decoupling problem. With a linearized perturbation analysis, he points out that the constant interaction of perturbed pressure and density fields contributes to the

catastrophic shock capturing of the approximate Riemann solver. He suggests a hybrid method that combines a low diffusion Riemann solver and a more dissipative one to improve the robustness. Pandolfi and D'Ambrosio [3] extend Quirk's linearized algorithm to a large collection of upwind schemes, they also concentrate on analyzing the interaction of pressure and density perturbations. It is important to note that carbuncle-free schemes such as the HLLE scheme [4] and the Van Leer's FVS scheme [5] damp density perturbation. By a similar linear stability analysis, Gressier and Moschetta [6] examine the damping properties of several Godunov-type Riemann solvers for the odd–even decoupling. A useful criterion is proposed which states that the strict stability and the exact resolution of contact discontinuities are not compatible. These works have a common argument that the instability results from the undamped density perturbations, so an approximate Riemann solver diminishing contact waves is able to avoid the carbuncle flaw. However, there are still some other Riemann solvers such as those in [7–10] which are able to resolve the stationary contact discontinuity exactly while still being free from the carbuncle. By closely examining these schemes, we find that these schemes give no smearing on contact waves, but they actually damp shear waves. In [11], the authors conduct the linearized analysis of Pandolfi and D'Ambrosio [3] on several upwind schemes for the odd–even decoupling problem. The results of these Riemann solvers show that a scheme giving dissipation on shear waves is free from the odd–even decoupling and the carbuncle. This indicates that the shock instability is strongly related to linear shear waves, which is also supported by works from Sanders et al. [12] and recently from Shen et al. [8,13]. There is a large collection of works considering modifying low diffusion Riemann solvers to resolve strong shock stably with the help of additional multidimensional dissipation, but few of them provide much insight into the carbuncle mechanism. It needs to be clarified why certain kind of dissipation is helpful to suppress the shock instability but others are not and what the underlying mechanism of suppressing the shock instability by multidimensional dissipation is.

Liou [14] argues that the root of causing the shock instability is the pressure difference in the dissipative term that appears in the numerical evaluation of convective fluxes. Based on a series of numerical experiments for various numerical schemes, he presents the conjecture: "A scheme having the property $D^{(p)} = 0$ in the mass flux is a shock-stable scheme". Here $D^{(p)} = 0$ is the dissipative pressure term in the mass flux. Following the same spirits of Liou's conjecture, Kim et al. [15] modify the pressure term in Roe's solver to balance damping and feeding rates between pressure and density fields. In [16,17], the authors manage to eliminate the pressure term in the mass flux by hybridizing the HLL scheme [18] and the HLLC scheme [19]. However, some researchers report several counterexamples to Liou's conjecture. For example, the flux splitting scheme HLL-CPS-Z [7], the HLLCM scheme [8], the LRS scheme [20] and even the AUSM+ scheme [21]. The first three Riemann solvers have one common property: they are all robust against the shock instability but own a dissipative pressure term in the mass flux. The last one, on the contrary, owns no pressure term in the mass flux, but it has been observed not to be carbuncle-free [3]. Although, as discussed in [8], Liou's conjecture does not identify correctly the source of the numerical instability, the pressure difference does play an important role in triggering or amplifying the unstable mode. Xu and Li [22] give a qualitative explanation of the shock instability. They point out that the coupling of perturbed velocity and pressure inside the numerical shock structure promotes the unstable mode and the Riemann solvers giving inadequate shear viscosity cannot reduce the velocity differences and stabilize the numerical shock structure. In the present study, we will show that the perturbed pressure appearing inside the numerical shock structure will be transported downstream in acoustic and entropy waves. That will lead to the inconsistency of mass flux across the normal shock (i.e., the mass flux behind the shock is not equal to that in front), which is considered to be the cause of the shock instability. The perturbed pressure will even be transported in the direction parallel to that of the shock front, resulting in a wedge-shaped shock profile.

The shock wave is considered as a jump discontinuity in terms of continuum mechanics on which the Euler equations are established. However, a physical shock wave has some finite width which is on the order of the particle mean free path. In order to capture the shock wave, artificial dissipation included in the numerical procedure is required to form the numerical shock structure in the grid scale. However, there is no clear physical interpretation of these intermediate states inside the numerical shock structure. Michael Dumbser et al. [23] and Chauvat et al. [24] analyze the shock instability with a matrix-based method. They find that the numerical instabilities of Riemann solvers for multidimensional steady normal shock are strongly related to the numerical shock structure. Such observations are also confirmed by the numerical results from Kitamura et al. [25]. Zaide and Roe [26] link the carbuncle of shock-capturing methods to the nonlinearity of the Hugoniot curve. They argue that these intermediate states inside captured shocks should not be assumed as being in local thermodynamic equilibrium. By introducing the interpolated fluxes that do not depend on untrustworthy intermediate cells, they propose two new flux functions that can give unambiguous stationary shock structures. Kitamura and Shima [27] also notice the importance of the numerical shock structure. Based on a series of numerical experiments on one and two-dimensional normal shock problems, they clarify the role of interfacial speed of sound and argue that the dissipation inside the shock structure should be proportional to the Mach number. Such work essentially adjusts the viscosity on the numerical shock structure to stabilize the scheme, but there is a common flaw that the shock is inevitably broadened to some extent. In the current study, the importance of the numerical shock structure is also emphasized, we will show that the unstable errors are generated from these unphysical states inside the numerical shock structure and then they are further amplified or damped due to different dissipative properties of Riemann solvers. Such a conclusion is different from those in the previous work by Dumbser et al. [23] and Xu [28] who suppose that the shock instability originates from the upstream or the downstream region respectively.

It is a widely acknowledged fact that diffusive Riemann solvers which give excessive dissipation on contact waves and shear waves are robust against the shock instability. But little work has been conducted to clarify which kind of linear
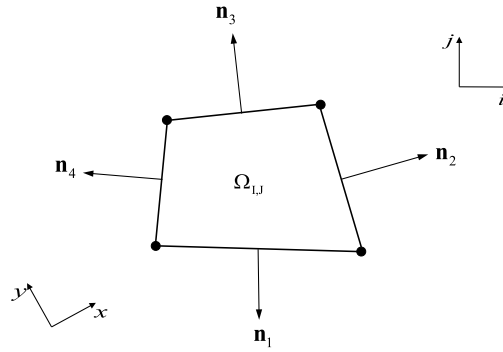
Fig. 1. Control volume for a structured grid in two dimensions.

dissipation is really responsible and how the corresponding dissipation plays a part in curing the instability. In the current study, the shock instability of several Godunov-type schemes in a unified framework is analyzed. We focus on the dissipative property and its connection to the unstable behavior. Through numerical experiments and a linearized analysis method, we will clarify which dissipative component is responsible for the instability and where the unstable errors are generated. The carbuncle mechanism is also discussed. Based on the observations from the results of numerical experiments and the linearized analysis, a simple cure for the shock instability is suggested and some numerical experiments for strong shock waves confirm its validity. The paper is organized as follows. Section 2 briefly reviews the Euler equations and the finite volume discretization. Section 3 presents four different Godunov-type Riemann solvers in a unified framework and their dissipative properties are also analyzed. A detailed analysis of shock instability for these Riemann solvers is given in Section 4. In Section 5, a shock-stable Riemann solver is presented. Numerical results of several strong shock wave problems are presented in Section 6 to assess the robustness of the proposed scheme. Finally, concluding remarks are made in Section 7.

2. Governing equations

The integral form of the two-dimensional Euler equations can be expressed as

$$\frac{\partial}{\partial t} \int_{\Omega} \mathbf{U} d\Omega + \oint_{\partial \Omega} \mathbf{F} dS = 0 \tag{1}$$

where $\partial \Omega$ denotes the boundary of the control volume Ω, $\mathbf{U}$ is the vector of conservative variables and $\mathbf{F}$ is the vector of convective fluxes, they are defined as

$$\mathbf{U} = \begin{pmatrix} \rho \\ \rho u \\ \rho v \\ E \end{pmatrix}, \quad \mathbf{F} = \begin{pmatrix} \rho q_n \\ \rho u q_n + n_x p \\ \rho v q_n + n_y p \\ q_n(E + p) \end{pmatrix}, \tag{2}$$

where ρ is the density, $\mathbf{u} = (u, v)$ is the flow velocity, p is the pressure and E is the total energy. q_n is the velocity normal to the surface element dS, i.e., $q_n \equiv \mathbf{u} \cdot \mathbf{n} = n_x u + n_y v$. $\mathbf{n} = n_x i + n_y j$ is the outward unit vector normal to the surface. The equation of state is in the form

$$p = (\gamma - 1) \rho e = (\gamma - 1) \left[E - \frac{1}{2} \rho \left(u^2 + v^2 \right) \right] \tag{3}$$

where γ is the specific heat ratio.

We consider a two-dimensional domain in $x - y$ space and assume it is subdivided into a number of structured quadrilateral cells. A particular volume $\Omega_{I,J}$ is displayed in Fig. 1. The governing equations are discretized using a cell-centered finite volume method as

$$\frac{d \overline{\mathbf{U}}_{I,J}}{dt} = -\frac{1}{|\Omega_{I,J}|} \sum_{m=1}^{N_F} \mathbf{F}_m \Delta S_m \tag{4}$$

In the above expression, the indices in capital letters (I, J) represent the control volume, $\overline{\mathbf{U}}_{I,J}$ is the cell average of $\mathbf{U}$ on $\Omega_{I,J}$, and $|\Omega_{I,J}|$ denotes the volume of $\Omega_{I,J}$. N_F denotes the number of control volume faces (which is $N_F = 4$ in 2D). ΔS_m is the length of S_m, $\mathbf{F}_m$ is the flux at the midpoint of S_m.
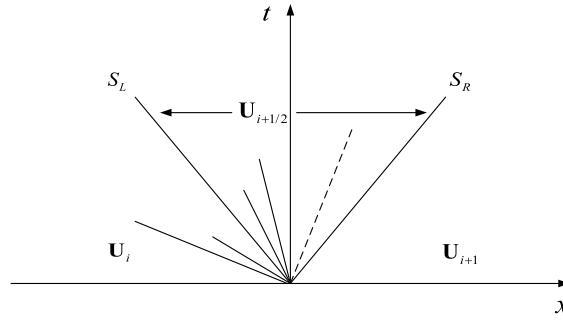
Fig. 2. The approximate solution of the Riemann problem.

3. Godunov-type Riemann solvers

The numerical flux $\boldsymbol{\Phi}_m$ across each interface m, may be determined by solving exactly or approximately a Riemann problem based on the one-dimensional Euler equation along the normal direction of the face S_m, i.e., $\mathbf{n}_m$,

$$\frac{\partial \mathbf{U}}{\partial t} + \frac{\partial \mathbf{F}_{n_m}}{\partial n_m} = 0 \tag{5}$$

with the initial data, $\mathbf{U}_L$ and $\mathbf{U}_R$ separated by the control volume interface. In what follows, we omit the subscript m for clarity.

3.1. The HLLE and HLLEM Riemann solvers

In this paper, we concentrate on analyzing the dissipative properties and their connections to the shock instabilities of a family of Godunov-type Riemann solvers. Firstly, two classical schemes: the HLLE scheme [4] and the HLLEM scheme [4,29] are reviewed.

Concerning the stability and the positivity preserving property, Einfeldt et al. [4,29] propose numerical approximations for the largest and smallest physical signal velocities in the exact solution to the Riemann problem. The resulting HLLE scheme (Harten–Lax–van Leer–Einfeldt) captures the shock profile sharply and does not admit an entropy violating jump in the expansion region where the flow becomes sonic. The wave structure of this approximate solution of the Riemann problem is illustrated in Fig. 2, where S_L, S_R are the smallest and largest signal velocities arising from the solution of the Riemann problem. The middle wave is a contact discontinuity included in the star region between S_L and S_R. However, the HLLE scheme omits the middle wave, hence this approximation consists of just three constant states separated by two waves. As a result, the scheme gives poor resolutions of contact discontinuities and shear waves. The HLLE scheme can be written by

$$\boldsymbol{\Phi}_{\text{HLLE}} = \frac{S_R \mathbf{F}_n(\mathbf{U}_L) - S_L \mathbf{F}_n(\mathbf{U}_R)}{S_R - S_L} + \frac{S_L S_R}{S_R - S_L} (\mathbf{U}_R - \mathbf{U}_L) \tag{6}$$

The wave speed estimates for S_L and S_R are defined as

$$S_L = min(0, (q_n)_L - a_L, \widehat{q}_n - \widehat{a}), \quad S_R = max(0, (q_n)_R + a_R, \widehat{q}_n + \widehat{a}) \tag{7}$$

where $(q_n)_{L,R} = (u, v)_{L,R} \cdot \mathbf{n}$, a_L and a_R denote the speeds of sound at the left and right sides, respectively, and $\widehat{(\cdot)}$ are Roe's averaged variables.

The HLLEM scheme is built on top of the existing HLLE scheme, thereby enjoying the excellent properties of the HLLE method. Furthermore, it improves the resolution of the contact discontinuity with the help of the so-called anti-diffusion terms in the linear degenerate fields. It can produce comparative solutions with modern approximate Riemann solvers such as the Roe-type and HLLC-type schemes. Actually, the HLLEM scheme not requiring an entropy fix can also be regarded as an improved version of the famous Roe scheme [30], because particular choices of anti-diffusion parameters and wave speed estimates reduce the HLLEM scheme to a Roe's solver. In addition, unlike the Riemann solvers of Roe and Osher [31], for the HLLEM scheme, the anti-diffusion terms added to the HLLE scheme can be evaluated with only the intermediate eigenvalues and the associated left and right eigenvectors without knowing the entire eigenstructure of the hyperbolic system. Recently, it has been extended to non-conservative hyperbolic systems and to general nonlinear hyperbolic systems of conservation laws [32]. Whereas, in the current study, we only consider the HLLEM scheme for conventional Euler systems. The HLLEM scheme can be written by

$$\boldsymbol{\Phi}_{\text{HLLEM}} = \frac{S_R \mathbf{F}_n(\mathbf{U}_L) - S_L \mathbf{F}_n(\mathbf{U}_R)}{S_R - S_L} + \frac{S_L S_R}{S_R - S_L} \left(\mathbf{U}_R - \mathbf{U}_L - \delta_2 \widehat{\alpha}_2 \widehat{\mathbf{R}}_2 - \delta_3 \widehat{\alpha}_3 \widehat{\mathbf{R}}_3 \right) \tag{8}$$

where $\widehat{\mathbf{R}}_k$ denote the right eigenvectors of the flux Jacobian evaluated at the intermediate states $\widehat{\mathbf{U}}$. $\widehat{\alpha}_k$ are the approximate values of the projection from $\mathbf{U}_R - \mathbf{U}_L$ onto $\widehat{\mathbf{R}}_k$, i.e.,

$$\mathbf{U}_R - \mathbf{U}_L = \sum_{k=1}^{4} \widehat{\alpha}_k \widehat{\mathbf{R}}_k \tag{9}$$

with

$$\widehat{\alpha}_{1,4} = \frac{\Delta p \pm \widehat{\rho}\,\widehat{a}\Delta q_n}{2\widehat{a}^2}, \quad \widehat{\alpha}_2 = \Delta \rho - \frac{\Delta p}{\widehat{a}^2}, \quad \widehat{\alpha}_3 = \widehat{\rho}(n_y \Delta u - n_x \Delta v) \tag{10}$$

and

$$\widehat{\mathbf{R}}_{1,4} = \begin{bmatrix} 1 \\ \widehat{u} \pm n_x \widehat{a} \\ \widehat{v} \pm n_y\,\widehat{a} \\ \widehat{H} \pm \widehat{a}\,\widehat{q}_n \end{bmatrix}, \qquad \widehat{\mathbf{R}}_2 = \begin{bmatrix} 1 \\ \widehat{u} \\ \widehat{v} \\ \frac{\widehat{u}^2 + \widehat{v}^2}{2} \end{bmatrix}, \qquad \widehat{\mathbf{R}}_3 = \begin{bmatrix} 0 \\ -n_y \\ n_x \\ -\widehat{u}n_y + \widehat{v}n_x \end{bmatrix} \tag{11}$$

δ_2 and δ_3 are the anti-diffusion coefficients defined to take out excess dissipation in the linear degenerate fields, i.e.,

$$\delta_2 = \delta_3 = \frac{\widehat{a}}{\widehat{a} + |\widehat{q}_n|} \tag{12}$$

It should be noted that the approximate speed of the contact discontinuity $\widehat{q}_n$ in Eq. (12) is substituted for Roe's averaged velocity, which enhances the resolution of linear degenerate waves [33].

3.2. Two alternative HLL-type Riemann solvers

It is a well-known fact that flux functions that are able to capture contact and shear discontinuities with minimal smearing are vulnerable to shock instability problems. Many researchers have reported that numerical dissipation corresponding to linear degenerate waves may be effective to alleviate the shock instability. There are two kinds of numerical dissipation associated with linear waves: one corresponding to the entropy wave and the other one corresponding to the vorticity wave. However, little work has concentrated on exploring which type of dissipation is really responsible for suppressing the shock instability. Here we define two alternative Riemann solvers in the framework of the HLLE and HLLEM schemes. The two new HLL-type Riemann solvers are constructed by selectively recovering the information of linear degenerate waves. They provide a convenient way to analyze the influence of different kinds of dissipation on the shock instability.

The Riemann problem of system (5) is considered. For the sake of brevity, the normal direction at the interface is assumed as $\boldsymbol{n}_m = (1, 0)$, i.e., the x direction. The solution of the Riemann problem at the interface $x_{i+1/2}$ is

$$\boldsymbol{\omega}_{i+1/2}\left[(x - x_{i+1/2})/(t - t^n)\right] \tag{13}$$

which depends only on the states $\mathbf{U}_i$, $\mathbf{U}_{i+1}$ and the ratio $(x - x_{i+1/2})/(t - t^n)$. For the HLLE scheme, the approximate solution consists of three constant states, i.e.,

$$\boldsymbol{\omega}_{i+1/2}(x'/t) = \begin{cases} \mathbf{U}_i & x'/t < S_{L,i+1/2} \\ \mathbf{U}_{i+1/2} & S_{L,i+1/2} < x'/t < S_{R,i+1/2} \\ \mathbf{U}_{i+1} & x'/t > S_{R,i+1/2} \end{cases} \tag{14}$$

where $x' = x - x_{i+1/2}$ and $S_{L,i+1/2}$, $S_{R,i+1/2}$ are the approximations to the smallest and largest physical signal velocities as shown in Fig. 2. Furthermore, we assume that $t^n = 0$ for convenience.

Following Einfeldt's strategy [4], we only isolate the anti-diffusion term for the entropy waves first. It can be implemented by modifying the averaged state $\mathbf{U}_{i+1/2}$ in the solution of a Riemann problem as

$$\boldsymbol{\omega}_{\mathrm{HLLEC}} = \begin{cases} \mathbf{U}_i & x'/t < S_{L,i+1/2} \\ \mathbf{U}_{i+1/2} + (x - \widehat{q}_{n,i+1/2} \cdot t) \cdot \widehat{\delta}_{2,i+1/2} \cdot \widehat{\alpha}_{2,i+1/2} \cdot \widehat{\mathbf{R}}_{2,i+1/2} & S_{L,i+1/2} < x'/t < S_{R,i+1/2} \\ \mathbf{U}_{i+1} & x'/t > S_{R,i+1/2} \end{cases} \tag{15}$$

The corresponding Riemann solver which is denoted as HLLEC can be written by

$$\boldsymbol{\Phi}_{\mathrm{HLLEC}} = \frac{S_R \mathbf{F}_n(\mathbf{U}_L) - S_L \mathbf{F}_n(\mathbf{U}_R)}{S_R - S_L} + \frac{S_L S_R}{S_R - S_L}(\mathbf{U}_R - \mathbf{U}_L - \delta_2 \widehat{\alpha}_2 \widehat{\mathbf{R}}_2) \tag{16}$$

Similarly, if only the anti-diffusion term for the shear waves is isolated, the resulting solution of the Riemann problem can be obtained,

Table 1
Definitions of Godunov-type flux functions.

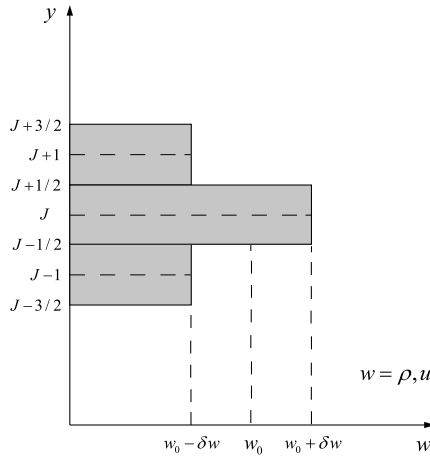|	HLLEM	HLLEC	HLLES	HLLE
δ_2	$\widehat{a}/(\widehat{a}+|\widehat{q}_n|)$	$\widehat{a}/(\widehat{a}+|\widehat{q}_n|)$	0	0
δ_3	$\widehat{a}/(\widehat{a}+|\widehat{q}_n|)$	0	$\widehat{a}/(\widehat{a}+|\widehat{q}_n|)$	0

Fig. 3. Graphic illustrations of stationary discontinuities.

$$\boldsymbol{\omega}_{\text{HLLES}} = \begin{cases} \mathbf{U}_i & x'/t < S_{L,i+1/2} \\ \mathbf{U}_{i+1/2} + (x - \widehat{q}_{n,i+1/2} \cdot t) \cdot \widehat{\delta}_{3,i+1/2} \cdot \widehat{\alpha}_{3,i+1/2} \cdot \widehat{\mathbf{R}}_{3,i+1/2} & S_{L,i+1/2} < x'/t < S_{R,i+1/2} \\ \mathbf{U}_{i+1} & x'/t > S_{R,i+1/2} \end{cases} \tag{17}$$

The corresponding Riemann solver which is denoted as HLLES can be written by

$$\boldsymbol{\Phi}_{\text{HLLES}} = \frac{S_R \mathbf{F}_n(\mathbf{U}_L) - S_L \mathbf{F}_n(\mathbf{U}_R)}{S_R - S_L} + \frac{S_L S_R}{S_R - S_L}(\mathbf{U}_R - \mathbf{U}_L - \delta_3 \widehat{\alpha}_3 \widehat{\mathbf{R}}_3) \tag{18}$$

3.3. Numerical dissipation analysis of the Godunov-type Riemann solvers

In the preceding section, two new Riemann solvers HLLEC and HLLES are constructed by selectively recovering the information of linearly degenerate waves. In order to clarify their dissipation mechanisms, the two solvers along with the HLLE scheme and the HLLEM scheme are expressed in a unified framework as Eq. (8). The only difference among these flux functions lies in the definitions of the anti-diffusion coefficients, which are demonstrated in Table 1.

In order to investigate the dissipative properties of the Riemann solvers in Table 1, we adopt the flux form which shows the numerical dissipation term explicitly,

$$\mathbf{F}_{1/2} = \frac{1}{2}(\mathbf{F}_L + \mathbf{F}_R) + \mathbf{D}_{1/2} \tag{19}$$

where L and R represent the left and right states, the average flux on the right hand side represents the central discretization of the flux terms and $\mathbf{D}_{1/2}$ represents the flux corresponding to the numerical diffusion. For the flux functions in (8), the corresponding $\mathbf{D}_{1/2}$ can be written as

$$\mathbf{D}_{1/2} = \frac{S_R + S_L}{2(S_R - S_L)}(\mathbf{F}_L - \mathbf{F}_R) + \frac{S_L S_R}{S_R - S_L}(\mathbf{U}_R - \mathbf{U}_L - \delta_2 \widehat{\alpha}_2 \widehat{\mathbf{R}}_2 - \delta_3 \widehat{\alpha}_3 \widehat{\mathbf{R}}_3) \tag{20}$$

Here, we consider two special and important cases. One is a stationary entropy wave and the other is a stationary shear wave, they are shown in Fig. 3. The discontinuities are set at the interface between the cell (I, J) and the cell $(I, J + 1)$. One should note that the unit normal vector at the interface is $\boldsymbol{n} = (n_x, n_y) = (0, 1)$. A simple entropy wave can be set up with an initial density jump, i.e.,

$$(\rho, u, v, p)_{I,K} = \begin{cases} (\rho_0 + \delta\rho, u_0, 0, p_0) & K = J \\ (\rho_0 - \delta\rho, u_0, 0, p_0) & K = J + 1 \end{cases} \tag{21}$$

where (ρ_0, u_0, v_0, p_0) are prescribed uniform conditions. For this case, the Roe's averaged normal velocity at the interface between cell (I, J) and cell $(I, J + 1)$ is $\widehat{q}_n = n_x \widehat{u} + n_y \widehat{v} = 0$. The corresponding dissipation term becomes

Table 2
Recursive formulas of Godunov-type flux functions (ν is the Courant number).

HLLEM	HLLEC	HLLES	HLLE
$\delta\rho^{n+1} = \delta\rho^n - \frac{2\nu}{\bar{a}^2} \cdot \delta p^n$	$\delta\rho^{n+1} = \delta\rho^n - \frac{2\nu}{\bar{a}^2} \cdot \delta p^n$	$\delta\rho^{n+1} = (1-2\nu) \cdot \delta\rho^n$	$\delta\rho^{n+1} = (1-2\nu) \cdot \delta\rho^n$
$\delta u^{n+1} = \delta u^n$	$\delta u^{n+1} = (1 - 2\nu\rho_0) \cdot \delta u^n$	$\delta u^{n+1} = \delta u^n$	$\delta u^{n+1} = (1-2\nu\rho_0) \cdot \delta u^n$
$\delta p^{n+1} = (1-2\nu) \cdot \delta p^n$	$\delta p^{n+1} = (1-2\nu) \cdot \delta p^n$	$\delta p^{n+1} = (1-2\nu) \cdot \delta p^n$	$\delta p^{n+1} = (1-2\nu) \cdot \delta p^n$

$$\mathbf{D}_{1/2}|_1 = -\frac{2S_L S_R}{S_R - S_L}[(1-\delta_2) \cdot \delta\rho] \tag{22}$$

It can be obtained from Eq. (22) that the sufficient condition for the numerical flux to accurately resolve the stationary entropy wave without dissipation is

$$\delta_2 = 1 \tag{23}$$

Through the close examination of the anti-diffusion coefficients of the Godunov-type schemes in Table 1, it can be observed that the HLLEM scheme and the HLLEC scheme both satisfy the condition (23) and give no dissipation for the stationary entropy wave.

Then we also need to consider the dissipation of the flux functions corresponding to the shear wave. Similarly, a simple stationary shear wave can be set up with a transversal velocity discontinuity, i.e.,

$$(\rho, u, v, p)_{I,K} = \begin{cases} (\rho_0, u_0 + \delta u, 0, p_0) & K = J \\ (\rho_0, u_0 - \delta u, 0, p_0) & K = J+1 \end{cases} \tag{24}$$

One should note that, in this problem, v is the velocity component normal to the interface, while u is acting as the shear velocity. The dissipation term can be derived as

$$\mathbf{D}_{1/2}|_2 = -\frac{2S_L S_R}{S_R - S_L}[(1-\delta_3)\rho_0 \cdot \delta u] \tag{25}$$

Similarly, it can be obtained from Eq. (25) that the sufficient condition for the numerical flux to accurately resolve the shear wave without dissipation is

$$\delta_3 = 1 \tag{26}$$

It can be observed that the HLLEM scheme and the HLLES scheme as designed both satisfy the condition (26) and give no dissipation for the stationary shear wave.

In order to further clarify the capabilities of these Riemann solvers to damp perturbations, we assume that the two-dimensional computational grid is uniform and the discrete solutions at time t^n are given by

$$\rho_J^n = \rho_0 + \delta\rho^n, \quad p_J^n = p_0 + \delta p^n, \quad u_J^n = u_0 + \delta u^n, \quad v_J^n = v_0 \tag{27}$$

and

$$\rho_{J\pm1}^n = \rho_0 - \delta\rho^n, \quad p_{J\pm1}^n = p_0 - \delta p^n, \quad u_{J\pm1}^n = u_0 - \delta u^n, \quad v_{J\pm1}^n = v_0 \tag{28}$$

Similar to the above analysis of the stationary entropy wave (21) and the stationary shear wave (24), the linearized analysis method in [3] is applied to clarify how the four Godunov-type schemes defined by (19), (20) and Table 1 damp out small perturbations. Table 2 shows the recursive formulas of different Godunov-type schemes. The results in Table 2 give a demonstration of how the perturbations are damped during the time-marching procedure due to the different numerical dissipation properties of Riemann solvers.

In summary, with the help of proper anti-diffusion terms, the HLLEM scheme captures both entropy waves and shear waves accurately. The HLLEC scheme captures entropy waves accurately and damps shear waves severely. On the contrary, the HLLES scheme captures shear waves accurately and damps entropy waves. The HLLE scheme introduces excessive dissipation on all intermediate waves. In the next section, the robustness of these four variants of the Godunov-type schemes in capturing a steady normal shock will be evaluated. By carrying out numerical experiments and a linearized analysis, the connections between the numerical dissipation and the shock instability properties of the Godunov-type schemes are explored in depth.

4. A shock instability analysis

4.1. Numerical experiment setup

The most reliable way to evaluate the robustness of numerical schemes to capture shock waves is to conduct numerical tests. The test conducted here is the steady normal shock wave problem in a two-dimensional rectangular domain that is
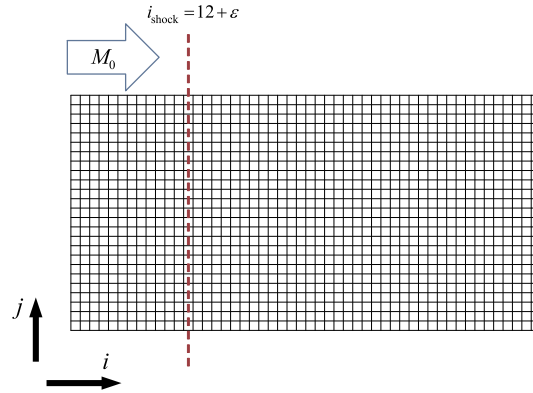
Fig. 4. Computational grid and conditions for Kitamura's steady normal shock test.

proposed by Kitamura et al. [25]. It has been widely used to evaluate the robustness of various shock-capturing schemes. It is believed that numerical schemes that produce shock instabilities for the steady normal shock test also produce carbuncle solutions for the blunt body problem [23,25,39]. In the subsequent sections, we will show that the Godunov-type schemes studied here have different instability characteristics due to their various dissipation mechanisms. For the convenience of a further discussion, we describe the numerical experiment setup in [25] once more and add some details.

As shown in Fig. 4, the computational grid comprises 50×25 cells evenly spaced without perturbations. The initial conditions are prescribed for left ($L : i \leq 12$) and right ($R : i \geq 14$) following the Rankine–Hugoniot conditions across the normal shock as:

$$\boldsymbol{U}_L = \begin{pmatrix} 1 \\ 1 \\ 0 \\ \frac{1}{\gamma(\gamma-1)M_0^2} + \frac{1}{2} \end{pmatrix}, \quad \boldsymbol{U}_R = \begin{pmatrix} f(M_0) \\ 1 \\ 0 \\ \frac{g(M_0)}{\gamma(\gamma-1)M_0^2} + \frac{1}{2f(M_0)} \end{pmatrix}, \tag{29}$$

where

$$f(M_0) = \left(\frac{2}{(\gamma+1)M_0^2} + \frac{\gamma-1}{\gamma+1} \right)^{-1}, \quad g(M_0) = \frac{2\gamma M_0^n}{\gamma+1} - \frac{\gamma-1}{\gamma+1}. \tag{30}$$

The freestream Mach number is $M_0 = 6.0$. As with the Roe scheme, the HLLEM scheme captures the shock with only one-internal point that belongs to a Hugoniot curve. The internal shock conditions ($M : i = 13$) are as follows [24]:

$$\begin{aligned} \rho_M &= (1-\alpha_\rho)\rho_L + \alpha_\rho \rho_R \\ u_M &= (1-\alpha_u)u_L + \alpha_u u_R \\ p_M &= (1-\alpha_p)p_L + \alpha_p p_R \end{aligned} \tag{31}$$

where

$$\begin{aligned} \alpha_\rho &= \varepsilon \\ \alpha_u &= \varepsilon \left(1 + (1-\varepsilon)\frac{M_0^2-1}{1+(\gamma-1)M_0^2/2} \right)^{-1/2} \left(1 + (1-\varepsilon)\frac{M_0^2-1}{1-2\gamma M_0^2/(\gamma-1)} \right)^{-1/2} \\ \alpha_p &= 1 - (1-\varepsilon)\left(1 + \varepsilon\frac{\gamma+1}{\gamma-1}\frac{M_0^2-1}{M_0^2} \right)^{-1/2} \end{aligned} \tag{32}$$

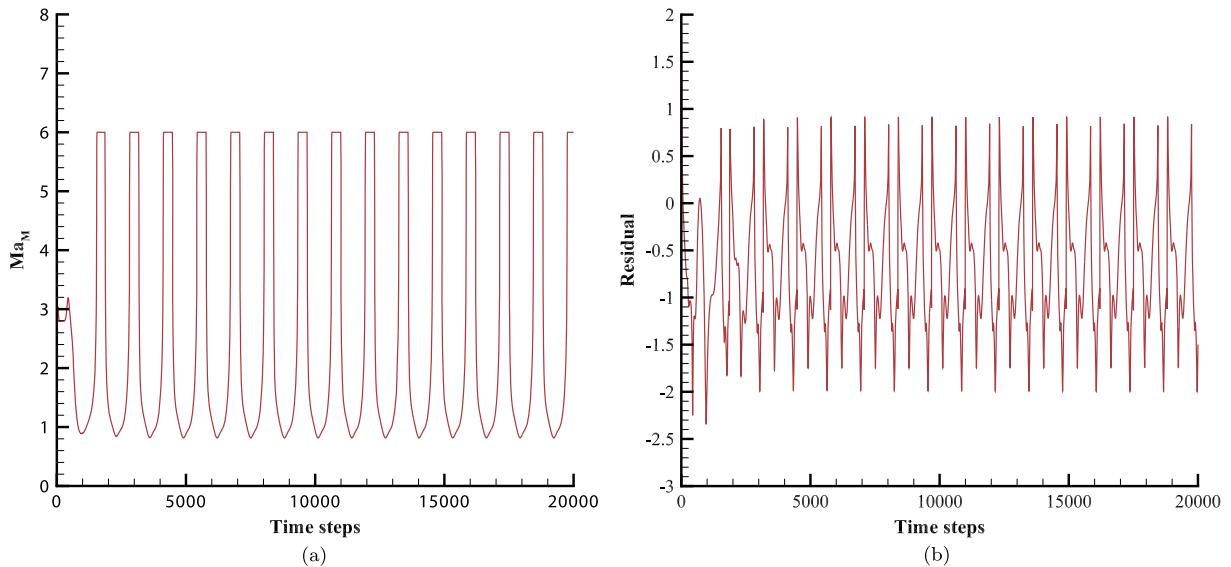The inflow boundary conditions are set to freestream values. The mass flux at the ghost cell is prescribed as

$$(\rho u)_{imax+1,j} = (\rho u)_0 = 1 \tag{33}$$

in order for the mass in the whole computational domain to remain constant and to fix the shock at the same position [34]. Meanwhile, other values are simply extrapolated. The periodical condition is imposed on the boundaries of j direction. The computations are conducted for 80,000 steps with CFL = 0.5. If a scheme is stable for all the shock positions ε, the scheme can be considered as shock-stable for this test.

Table 3
1D and 1.5D test results of Godunov-type flux functions (S: stable and converged, U: unstable).

Riemann solver	Test problem	$\varepsilon = 0.0$	0.1	0.2	0.3	0.4	0.5	0.6	0.7	0.8	0.9
HLLEM	1D	U	U	U	U	S	S	S	S	S	S
	1.5D	U	U	U	U	U	U	U	S	S	S
HLLEC	1D	U	U	U	U	S	S	S	S	S	S
	1.5D	S	S	S	S	S	S	S	S	S	S
HLLES	1D	U	U	U	U	S	S	S	S	S	S
	1.5D	U	U	U	U	U	U	U	S	S	S
HLLE	1D	U	U	U	U	S	S	S	S	S	S
	1.5D	S	S	S	S	S	S	S	S	S	S

Fig. 5. 1D shock instability predicted by the HLLEM scheme ($M_0 = 6.0$, $\varepsilon = 0.3$. Only the solutions before 20000 time steps are shown for clarity), (a) Mach number in cell M, (b) residual histories.

4.2. Steady normal shock results

In the present work, Kitamura's 1.5D numerical experiments are repeated to test the four different types of Riemann solvers. Its 1D counterparts where only one cell is used in the direction parallel to the shock wave are also conducted. A summary of the results is given in Table 3. It can be seen from the table that all the four Riemann solvers give the same shock instability results for the one-dimensional case, which are in accordance with their same nonlinear wave structures. Fig. 5 shows the unstable solutions of the 1D steady normal shock problem computed with the HLLEM scheme. Under the boundary condition based on a fixed mass flux, the resolved shock does not remain steady as the intermediate state keeps changing. The intermediate state enters into a limit cycle involving the shedding of spurious waves and their reflection from the downstream boundary, which is one of the main factors to trigger the multidimensional shock instability.

For the 1.5D test case, the HLLEC scheme and the HLLE scheme pass the tests for all shock positions, these two schemes both have dissipation on shear waves. The HLLEM scheme and the HLLES scheme give the same test results, they both capture shear waves accurately. Compared with the HLLEM scheme, the HLLES scheme introduces dissipation on entropy waves, but such dissipation is not helpful in stabilizing the shock. However, the HLLEC scheme that only introduces the shear viscosity to the HLLEM scheme can give stable results for all shock positions. It can be concluded that the dissipation corresponding to shear waves is crucial to suppress the shock instability, whereas the dissipation corresponding to entropy waves is not enough to stabilize the shock wave.

The above conclusion is obtained by the numerical results of a family of HLLE-type schemes. In order to verify whether it is suitable for other Riemann solvers, the 1.5D test cases are repeated to test other various Riemann solvers with different dissipative mechanisms. In Table 4, a summary of the results of different schemes is shown. The recursive formulas which describe the schemes' dissipative behaviors to smear stationary contact and shear discontinuities are also given. It should be noted that two modified Roe schemes (i.e. Roe (E-fix1) and Roe (E-fix2)) with different dissipative properties are defined. By applying Harten's entropy fixes to eigenvalues corresponding to the contact waves or the shear waves, the Roe scheme is modified to smear contact or shear discontinuities in the same way that the HLLES scheme or the HLLEC scheme does respectively. In Appendix A, we provide the detailed definitions. In Table 4, these schemes are categorized into three groups. In the first group, three Riemann solvers: HLLES scheme, Roe scheme with Harten's entropy fix (E-fix1) [35,36] and

Table 4
1.5D test results of various flux functions and recursive formulas of density and shear velocity perturbations (S: stable and converged for all shock positions, U: unstable for certain shock positions).

	Scheme	Dissipative property	Shock stability
Group 1	HLLES Roe (E-fix1) HLLS	$\delta\rho^{n+1} = (1-2\nu)\cdot\delta\rho^n$ $\delta u^{n+1} = \delta u^n$	U
Group 2	HLLEC Roe (E-fix2) HLLCM AUFS HLL-CPS-Z	$\delta\rho^{n+1} = \delta\rho^n - \frac{2\nu}{\bar{a}^2}\cdot\delta p^n$ $\delta u^{n+1} = (1-2\nu\rho_0)\cdot\delta u^n$ $\delta\rho^{n+1} = \delta\rho^n - \frac{2\nu}{\bar{a}^2}\cdot\delta p^n$ $\delta u^{n+1} = \left(1 - \frac{2\nu\rho_0}{\bar{a}^2}\right)\cdot\delta u^n$	S
Group 3	Rusanov HLLE Steger–Warming's FVS Van Leer's FVS	$\delta\rho^{n+1} = (1-2\nu)\cdot\delta\rho^n$ $\delta u^{n+1} = (1-2\nu\rho_0)\cdot\delta u^n$ $\delta\rho^{n+1} = \left(1 - \frac{\nu}{\bar{a}^2}\right)\cdot\delta\rho^n - \frac{\nu}{\bar{a}^2}\cdot\delta p^n$ $\delta u^{n+1} = \left(1 - \frac{2\nu\rho_0}{\bar{a}^2}\right)\cdot\delta u^n$ $\delta\rho^{n+1} = \left(1 - \frac{\nu}{2}\right)\cdot\delta\rho^n - \frac{\nu}{2}\cdot\delta p^n$ $\delta u^{n+1} = (1-2\nu\rho_0)\cdot\delta u^n$	S

HLLS scheme [8] are tested. These three schemes have one common property: they damp contact waves but have minimal diffusion on shear waves. The result shows that these three schemes cannot give stable solutions for all shock positions. In the second group, five schemes: HLLEC scheme, Roe scheme with Harten's entropy fix (E-fix2), HLLCM scheme [8], AUFS scheme [9] and HLL-CPS-Z [7] are listed. In contrast to the schemes in group 1, they resolve stationary contact waves accurately but smear shear waves. The result shows that a scheme with shear wave dissipation can give stable solutions for the 1.5D test cases. In group 3, four schemes: Rusanov [37], HLLE [29], Steger–Warming's FVS [38] and Van Leer's FVS [5] are listed. They have dissipation on both contact waves and shear waves and give stable solutions for the tests. Such results of these numerical experiments further validate the conclusion that the dissipation corresponding to shear waves is crucial to suppress the shock instability, whereas the dissipation corresponding to contact waves is not enough to stabilize the shock wave for the 1.5D test case. In the subsequent sections, we will explain why shear wave dissipation can stabilize shocks with the help of further numerical experiments and a linearized analysis. What should be noted is that this conclusion is believed to probably also apply to other various Riemann solvers, the validity of the conclusion is only proved by numerical results of the Riemann solvers listed in Table 4.

A typical unstable solution of the Godunov-type schemes usually develops in three typical phases that are described first in references [1,39]. As shown in Fig. 6, at the beginning of the instability, a series of wiggles appears around the shock front itself. These wiggles shown by contour maps are caused by the inconsistency of flow variables in the transverse direction inside the numerical shock structure. Then it further develops into an intermediate stage characterized by a series of parallel jets of alternating high and low velocity behind the shock. With the magnitude of these velocity disturbances growing, some high or low pressure zones form around the shock accompanied with a wedge-shaped shock profile. This stage is called carbuncle. In the subsequent section, we will give a heuristic explanation of how this phenomenon forms with the help of a linearized perturbation analysis.

4.3. Causes of the shock instability

The experimental results of different Riemann solvers indicate that the shock instability characteristics are strongly related to the numerical dissipative properties of Riemann solvers. In order to understand the mechanism of the shock instability, we need to clarify two important issues first. One is the spatial location of the source of instability, the other is which error component is responsible for the shock instability. To resolve such puzzles, a series of numerical experiments is carried out.

The basic experiment setup is described in section 4.1, the HLLEM scheme is selected to be the testing scheme due to its low diffusion property and poor robustness against the shock instability. The computations are conducted until time steps reach 80,000, the CFL number is 0.5 and the unstable shock position is chosen to be $\varepsilon = 0.3$. In addition, four different artificial restrictive conditions are prescribed respectively at three "dangerous" cells (see the cells filled with shadow in Fig. 7) during the time-marching procedure. These restrictive conditions are proposed with the knowledge that the instability is strongly related to how the shock is resolved. Zaide and Roe [26] argue that the shock instabilities of Riemann solvers are closely related to the nonlinearity of the Rankine–Hugoniot jump conditions. Therefore, these three "dangerous" cells, i.e. the cell just before the shock in the upstream region, the one inside the shock structure and the one just behind the shock in the downstream region should be carefully investigated. The detailed formulations and results are summarized in Table 5. In the table, the symbols $(\cdot)_L^n$, $(\cdot)_M^n$ and $(\cdot)_R^n$ denote states in cells L, M and R respectively at time t^n. Similarly, the symbols $(\cdot)_L^0$ and $(\cdot)_R^0$ denote states in cells L and R respectively at the initial moment.
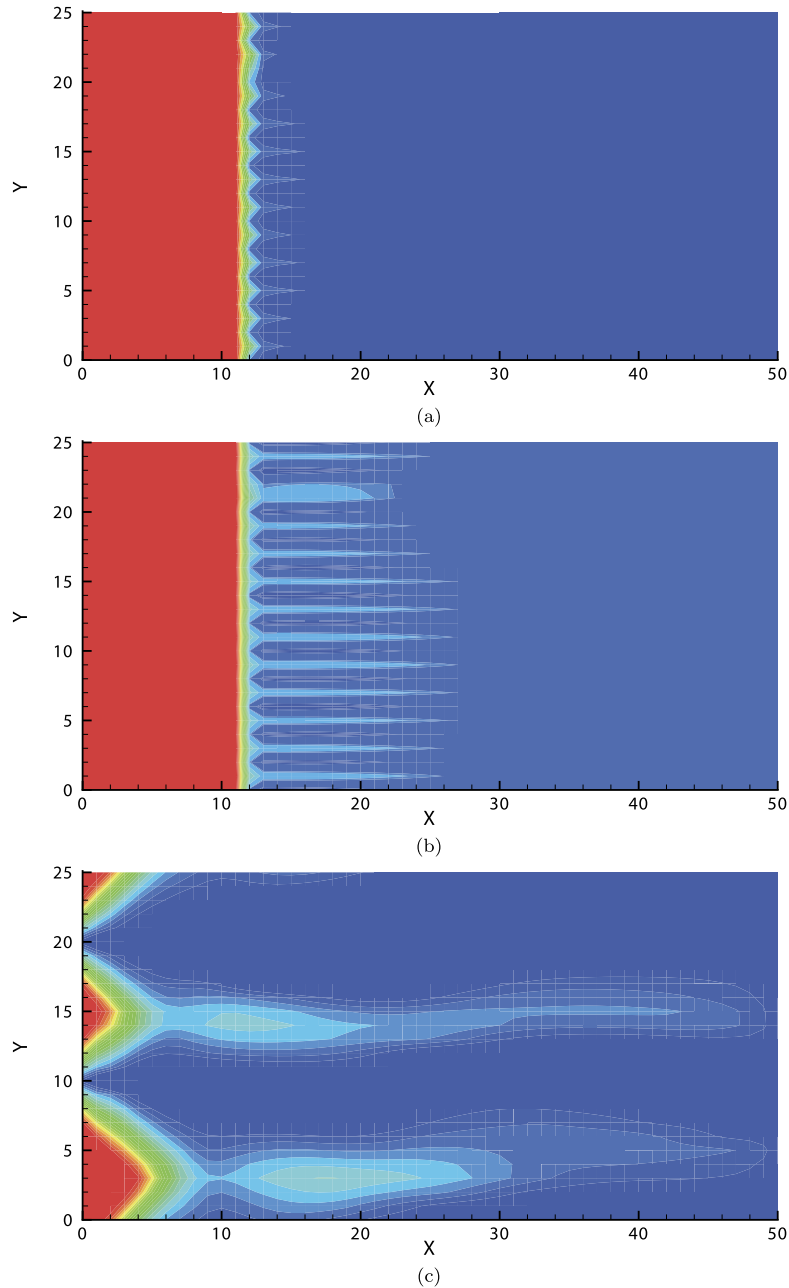
Fig. 6. Three stages of the shock instability: Mach number contours, (a) the initial stage at 200 time steps, (b) the second stage at 300 time steps, (c) the third stage at 1800 time steps.

Under the condition A, the states in cell L are fixed to the initial conditions in the upstream region of the shock, that is, no perturbations appear in cell L during the time-marching procedure. However, the instabilities still happen for both 1D and 1.5D cases. It implies that the shock instability cannot originate from the cell in the upstream region, otherwise the solutions of numerical tests under the condition A should be stable. Actually, in a normal test where no artificial restrictive conditions are prescribed, there are no perturbations appearing in the upstream region of the shock during the computations. To give a detailed illustration, we provide the solutions in cell L of the 1D shock instability case in Fig. 8. It clearly demonstrates that the states in cell L are always equal to the initial states during the computations.

The condition B is designed to fix the intermediate states to stable steady solutions inside the shock structure, no perturbations appear in cell M during the computations. The results show that the normal shock is stabilized. Such fact implies that these perturbations inside the shock structure are the main factors to trigger the instability. Furthermore, in this case, the states in cell L and cell M are both stable steady solutions and the states in the downstream cells are
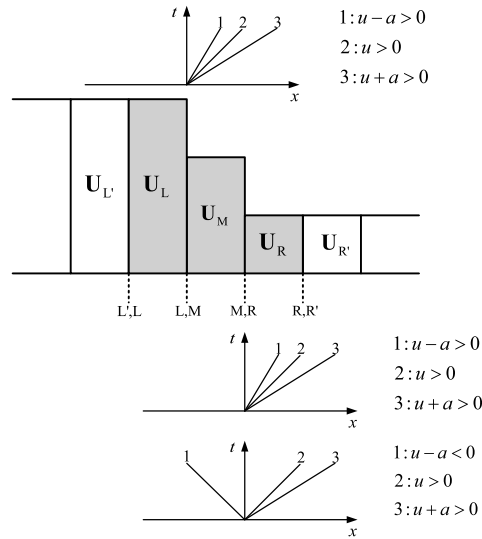
Fig. 7. The numerical shock structure and wave patterns for unstable cases.

Table 5
Summary of computed results of the HLLEM scheme for 1D and 1.5D steady shock problems with various constraints ($M_0 = 6.0$, $\varepsilon = 0.3$; S: stable and converged, U: unstable).

No.	A	B	C	D
Constraints	$\mathbf{U}_L^n = \mathbf{U}_L^0$	$\mathbf{U}_M^n = \mathbf{U}_M^{*\,a}$	$\mathbf{U}_R^n = \mathbf{U}_R^0$	$(\rho u)_R^n = (\rho u)_L^0$
1D	U	S	S	S
1.5D	U	S	S	S

[a] $\mathbf{U}_M^*$ are the stable solutions in cell M which are obtained from the results with constraint C.
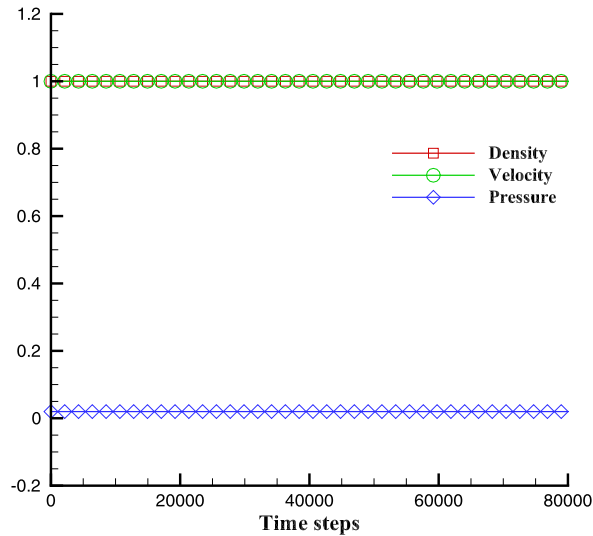

Fig. 8. Solutions of the HLLEM scheme in cell L for 1D shock instability case ($M_0 = 6.0$, $\varepsilon = 0.3$. Only one out of two thousand symbols are drawn in the picture for clarity).

not restricted by any artificial conditions. Hence, if an instability happens, the perturbations can only be generated from the downstream cells. The solution is stable for the numerical test under the condition B, so it can be deduced that the instability cannot originate from the downstream region of the shock.

The conditions C and D are designed to analyze how the perturbations appearing in cell M can influence the downstream region and how the perturbations in cell R can influence the stability. Under the condition C, the states in cell R are prescribed as the initial post shock conditions. It just cuts off the path of the propagation of spurious errors appearing in cell M, so the shock stabilizes. It also confirms that the instability is strongly related to the perturbations in cell M and

Table 6
Summary of computed results of different Riemann solvers for 1D and 1.5D steady shock problems with various constraints ("$\sqrt{}$" means that the scheme can give the same results for all shock positions as those of the HLLEM scheme in Table 5).

	$Ma = 6.0$		$Ma = 10.0$		$Ma = 20.0$		$Ma = 50.0$		$Ma = 100.0$	
	1D	1.5D	1D	1.5D	1D	1.5D	1D	1.5D	1D	1.5D
Godunov	$\sqrt{}$	$\sqrt{}$	$\sqrt{}$	$\sqrt{}$	$\sqrt{}$	$\sqrt{}$	$\sqrt{}$	$\sqrt{}$	$\sqrt{}$	$\sqrt{}$
Roe	$\sqrt{}$	$\sqrt{}$	$\sqrt{}$	$\sqrt{}$	$\sqrt{}$	$\sqrt{}$	$\sqrt{}$	$\sqrt{}$	$\sqrt{}$	$\sqrt{}$
HLLEM	$\sqrt{}$	$\sqrt{}$	$\sqrt{}$	$\sqrt{}$	$\sqrt{}$	$\sqrt{}$	$\sqrt{}$	$\sqrt{}$	$\sqrt{}$	$\sqrt{}$
HLLC	$\sqrt{}$	$\sqrt{}$	$\sqrt{}$	$\sqrt{}$	$\sqrt{}$	$\sqrt{}$	$\sqrt{}$	$\sqrt{}$	$\sqrt{}$	$\sqrt{}$
AUSM+	$\sqrt{}$	$\sqrt{}$	$\sqrt{}$	$\sqrt{}$	$\sqrt{}$	$\sqrt{}$	$\sqrt{}$	$\sqrt{}$	$\sqrt{}$	$\sqrt{}$
AUSM+-up	$\sqrt{}$	$\sqrt{}$	$\sqrt{}$	$\sqrt{}$	$\sqrt{}$	$\sqrt{}$	$\sqrt{}$	$\sqrt{}$	$\sqrt{}$	$\sqrt{}$
AUSMPW+	$\sqrt{}$	$\sqrt{}$	$\sqrt{}$	$\sqrt{}$	$\sqrt{}$	$\sqrt{}$	$\sqrt{}$	$\sqrt{}$	$\sqrt{}$	$\sqrt{}$
SLAU	$\sqrt{}$	$\sqrt{}$	$\sqrt{}$	$\sqrt{}$	$\sqrt{}$	$\sqrt{}$	$\sqrt{}$	$\sqrt{}$	$\sqrt{}$	$\sqrt{}$
LDFSS	$\sqrt{}$	$\sqrt{}$	$\sqrt{}$	$\sqrt{}$	$\sqrt{}$	$\sqrt{}$	$\sqrt{}$	$\sqrt{}$	$\sqrt{}$	$\sqrt{}$

their downstream propagation. The condition D is proposed to be in accordance with the physical reality that the mass flux across the normal shock should be consistent, that is, the mass flux in cell R should be equal to that in cell L. The results show that the normal shock is stabilized when the mass flux is correctly preserved across the normal shock for both 1D and 1.5D cases. This result just supports the conclusion of Shen et al. [8,13] that the inconsistent normal momentum distribution in the transverse direction of shock wave is the source to cause the instability.

In order to examine whether those results of numerical experiments under different restrictive conditions in Table 5 are general, this series of numerical experiments is extended to other cases with different unstable shock positions and a wide Mach number spectrum. The maximum Mach number even reaches 100 although the Euler and Navier–Stokes equations may not be valid. Moreover, the flux functions are not limited to the HLLE-type schemes in the current study. In Table 6, we list the selected schemes. In addition to the HLLEM scheme, the table also includes Godunov's exact Riemann solver [40]; Roe's (original) scheme [30]; HLLC [19], AUSM+ [21], AUSM+-up [41], AUSMPW+ [42], SLAU [43] and LDFSS [44] schemes. They are known to resolve linear waves with minimal diffusion. Therefore, they are all plagued by one-dimensional and multidimensional instabilities. The numerical experiments under different restrictive conditions are repeated to test these schemes. The results show that all the schemes give the same results for different shock positions and a wide range of Mach numbers as those of the HLLEM scheme in Table 5. As a result, we have reached the following conclusions:

1. The perturbations of the shock instability originate from the intermediate states inside the numerical shock structure.
2. A scheme accurately preserving the mass flux across the normal shock is a shock-stable scheme.

Here, a shock-stable scheme means that the scheme can give stable and converged solutions for all shock positions in 1D and 1.5D steady normal shock problems. What should be noted is that such conclusions are believed to probably also apply to other various Riemann solvers, but the validity of the conclusions is only proved by numerical results of the Riemann solvers listed in Table 6.

4.4. Numerical dissipation and its connection to the shock instability

The above conclusions pave the way for a better understanding of how the shock instability happens. It can be speculated that the perturbations originate from the intermediate cell and then they are propagated downstream, resulting in the inconsistency of mass flux across the normal shock. Here, the inconsistency means that the mass flux in cell R is not equal to that in cell L during the computations, i.e. $(\rho u)_R^n \neq (\rho u)_L^n$. If a Riemann solver does not damp these perturbations, then a shock instability may happen. For the Riemann solvers in the current study, if an instability happens in the one dimension, these perturbations cannot be effectively damped. However, in a two-dimensional case, these perturbations can be damped by the multidimensional dissipation. This may be the reason why a Riemann solver with inherent multidimensional dissipation can stabilize the multidimensional shock while it still encounters the instability for the one-dimensional case in the same unstable position. The numerical results of Godunov-type schemes in section 4.2 show that different dissipative properties of Riemann solvers contribute differently to the shock instability. Here, the connection between the numerical dissipation of Riemann solvers and the shock instability is further explored.

The numerical experiments and their conclusions indicate that the one-dimensional shock instability and the multidimensional shock instability are closely connected although they may have different instability mechanisms. The multidimensional instability is a result of numerical nonlinear coupled convections of perturbations in both x and y directions. In the initial stage of the instability, the perturbations are small, the coupled convections of them are fairly weak. Hence, it is still reasonable to study the multidimensional instability by assuming that the convections are decoupled in the initial stage of the instability. Here, we focus on studying the behaviors of the numerical perturbations at the beginning of the instability.

First, we need to clarify the perturbation errors that contribute to the inconsistency of mass flux across the normal shock. Here, the perturbation errors which are assumed to be small in the analysis refer to the discrepancies between the perturbed states and the stable steady solutions. It can be speculated from the numerical experiments and their results that the perturbation errors are generated in the intermediate cell and then they are propagated downstream, leading to errors in the cells just behind the shock front, these errors cause the mass flux inconsistency across the normal shock. When the

multidimensional instability happens, due to different perturbation errors appearing, the states in the cells that are located in the transverse direction of shock are usually inconsistent. A Riemann solver with inherent dissipation will damp these errors, then a stable solution will be obtained. If the dissipation is not enough, such errors will be further amplified, ending up with an unstable result. Next, we will clarify this process with the help of a linearized perturbation analysis.

At time t^n, it is assumed that the instability happens and the intermediate states are perturbed. The mass flux in cell R in the next time level is updated from x-direction as

$$(\rho u)_R^{n+1} = (\rho u)_R^n - \frac{\Delta t}{\Delta x}\left[\left(\rho u^2 + p\right)_{R,R'}^n - \left(\rho u^2 + p\right)_{M,R}^n\right] \tag{34}$$

The subscript R, R' denotes the interface between the cell R and the cell R', the subscript M, R denotes the interface between the cell M and the cell R (see Fig. 7 for a detailed illustration). Here, there are two situations to be considered. In Fig. 7, wave patterns corresponding to the two situations at the interface M, R are illustrated. As shown, one case is the velocity at the interface M, R is supersonic and the other one is subsonic. We shall only discuss the subsonic case here, whereas the easier supersonic case can be done in a similar way.

For the flux function in (8), the numerical fluxes at the interfaces in Eq. (34) can be written as

$$\begin{aligned}
\left(\rho u^2 + p\right)_{R,R'}^n &= \left(\rho u^2 + p\right)_R^n, \\
\left(\rho u^2 + p\right)_{M,R}^n &= \frac{S_R}{S_R - S_M}\left(\rho u^2 + p\right)_M^n - \frac{S_M}{S_R - S_M}\left(\rho u^2 + p\right)_R^n \\
&\quad + \frac{S_M S_R}{S_R - S_M}\left[(\rho u)_R^n - (\rho u)_M^n - \delta_2\left(\rho_R^n - \rho_M^n - \frac{p_R^n - p_M^n}{\hat{a}^2}\right)\hat{u}\right].
\end{aligned} \tag{35}$$

Here, the subscript M denotes the cell M, the subscript R denotes the cell R that is at the right side of M. $\widehat{(\cdot)}$ are Roe's averaged variables between states in cell M and cell R. Note that the first relation in Eq. (35) is true because at time t^n the states in cell R and cell R' are unperturbed and thus they are identical. Inserting Eqs. (35) into Eq. (34), it can be obtained that

$$\begin{aligned}
(\rho u)_R^{n+1} = (\rho u)_R^n - \frac{\Delta t}{\Delta x}\bigg[&(\rho u)_R^n u_R^n + p_R^n - \frac{S_R}{S_R - S_M}(\rho u)_M^n u_M^n - \frac{S_R}{S_R - S_M}p_M^n \\
&+ \frac{S_M}{S_R - S_M}(\rho u)_R^n u_R^n + \frac{S_M}{S_R - S_M}p_R^n - \frac{S_M S_R}{S_R - S_M}(\rho u)_R^n + \frac{S_M S_R}{S_R - S_M}(\rho u)_M^n \\
&+ \frac{S_M S_R}{S_R - S_M}\delta_2\hat{u}\left(\rho_R^n - \rho_M^n - \frac{p_R^n - p_M^n}{\hat{a}^2}\right)\bigg]
\end{aligned} \tag{36}$$

At time t^n, the instability happens. It is assumed that there are some perturbation errors being generated in the cell M. These are

$$\rho_M^n = \rho_M^{*,n} + \delta\rho_M^n, \quad (\rho u)_M^n = (\rho u)_M^{*,n} + \delta(\rho u)_M^n, \quad p_M^n = p_M^{*,n} + \delta p_M^n. \tag{37}$$

where $(\cdot)^*$ denote the stable steady solutions that are assumed to locate at a Hugoniot curve. They have the following relationship with states in cell L and cell R.

$$\rho_M^{*,n} = (1 - \alpha_\rho)\rho_L^{*,n} + \alpha_\rho\rho_R^{*,n}, \quad u_M^{*,n} = (1 - \alpha_u)u_L^{*,n} + \alpha_u u_R^{*,n}, \quad p_M^{*,n} = (1 - \alpha_p)p_L^{*,n} + \alpha_p p_R^{*,n}, \tag{38}$$

where the coefficients α_ρ, α_u and α_p are defined in (32). Combining Eqs. (36), (37) and (38), we can obtain the following relationship (see Appendix B for more details)

$$\delta(\rho u)_R^{n+1} - \delta(\rho u)_R^n = \theta_\rho \cdot \delta\rho_M^n + \theta_u \cdot \delta u_M^n + \theta_p \cdot \delta p_M^n \tag{39}$$

with

$$\begin{aligned}
\theta_\rho &= \frac{S_R \nu M_0}{(S_R - S_M)(1 + M_0)}\left(\frac{\omega^2}{f^2} - \frac{S_M\omega}{f} + \frac{S_M\delta_2}{f}\frac{1 + \omega\sqrt{\sigma}}{1 + \sqrt{\sigma}}\right) \\
\theta_u &= \frac{S_R \nu M_0}{(S_R - S_M)(1 + M_0)}(2\sigma\omega - S_M\sigma f) \\
\theta_p &= \frac{S_R \nu M_0}{(S_R - S_M)(1 + M_0)}\left(1 - \frac{S_M\delta_2}{\hat{a}^2 f}\frac{1 + \sqrt{\sigma}\omega}{1 + \sqrt{\sigma}}\right)
\end{aligned} \tag{40}$$

where the coefficients θ_ρ, θ_u and θ_p are functions of the freestream Mach number M_0 and the shock position parameter ε. In Appendix B, we provide these detailed formulas.

Table 7

Erroneous mass fluxes of different Riemann solvers when the number of time steps goes to infinity.

	$\delta(\rho u)^{\infty}$
HLLEM	∞
HLLEC	∞
HLLES	∞
HLLE	$\delta(\rho u)_R^0 + \frac{S_R M_0}{2(S_R - S_M)(1 + M_0)} \left[\left(\frac{\omega^2}{f^2} - \frac{S_M \omega}{f} \right) \cdot \delta\rho_M^0 + (2\sigma\omega - S_M\sigma f) \cdot \delta u_M^0 + \delta p_M^0 \right]$

The Eq. (39) clarifies the perturbation errors that cause the perturbation of mass flux in cell R. The density perturbation, the normal velocity perturbation and the pressure perturbation all contribute to the mass flux perturbation in cell R. It can also be observed that the freestream Mach number M_0 and the shock position parameter ε play important roles in scaling these perturbations, because the coefficients of perturbation errors θ_ρ, θ_u and θ_p are functions of M_0 and ε (see Appendix B for the detailed formulas). In Fig. 9, three curved surfaces are plotted. They show how the coefficients of perturbation errors θ_ρ, θ_u and θ_p change with the freestream Mach number M_0 and the shock position parameter ε. As shown in Fig. 9, the coefficients generally increase with an increasing Mach number M_0 and a decreasing shock position parameter ε. That means the scheme is more prone to the shock instability at a high freestream Mach number and a small shock position parameter. Such observations are correspondent with the numerical experiment results in section 4.2 and the references [23–25]. There, the results of numerical experiments also show that the shock instability is easier to happen under a higher freestream Mach number and a smaller shock position parameter. However, one should note that the linearized analysis only works well at the initial stage of the shock instability where the perturbation errors are relatively small. Hence, it can only provide a qualitative prediction of the instability. Fig. 7 shows the wave patterns of the HLLEM scheme in the x-direction. Referring to wave patterns at the interface M, R, it can be obtained that these perturbation errors propagate downstream in entropy and acoustic waves. The wave pattern at the interface L, M indicates that these errors cannot propagate upstream due to the upwind property of the flux function. To give a detailed illustration, we provide the wave speed estimate $S_L = min(u_L - a_L, \hat{u} - \hat{a})$ of the flux function at the interface L, M in Fig. 10. As shown in Fig. 10, the left wave speed is always greater than zero, that is, the flow velocity at the interface L, M is always supersonic during the computations. Such a fact further supports the results in Fig. 8 in section 4.3 which indicate that the solutions in the upstream region remain unperturbed during the computations, because perturbation errors appearing in cell M cannot propagate upstream.

Following the dimensional splitting method, we begin analyzing the shock instability problem by considering the perturbation due to the update to the momentum component from x-direction. The numerical flux function in y-direction approximates the physical convection in this direction. If there are some perturbations appearing, the numerical viscosity of the flux function provides a dissipative mechanism that attempts to damp the perturbations. Although the perturbation errors actually develop in a complex nonlinear manner due to the coupled convections in both directions, it is still possible to examine the way in which a Riemann solver evolves the certain sets of initial errors produced by the intermediate states inside the numerical shock structure. In section 3.3, the recursive formulas of different Godunov-type schemes have been obtained. They describe how a Riemann solver evolves these initial perturbation errors with time along the y-direction. With different settings of the anti-diffusion coefficients, these Godunov-type schemes response differently to the perturbation errors in cell M. The recursive formulas of these Godunov-type Riemann solvers can be written in a unified form as

$$\delta\rho^{n+1} = [1 - 2\nu(1 - \delta_2)] \cdot \delta\rho^n - \frac{2\nu}{\hat{a}^2}\delta_2 \cdot \delta p^n$$
$$\delta u^{n+1} = [1 - 2\nu\rho_0(1 - \delta_3)] \cdot \delta u^n \tag{41}$$
$$\delta p^{n+1} = (1 - 2\nu) \cdot \delta p^n$$

where the coefficients δ_2 and δ_3 depend on which Riemann solver is chosen.

Inserting Eq. (41) into Eq. (39), the mass flux in cell R at time t^n can be obtained as

$$\delta(\rho u)_R^n = \delta(\rho u)_R^0 + \alpha \cdot \delta\rho_M^0 + \beta \cdot \delta u_M^0 + \gamma \cdot \delta p_M^0 \tag{42}$$

where the coefficients α, β and γ of these initial perturbation errors are determined by which Riemann solver is used. In Appendix C, we provide the detail formulas of Eq. (42) for these Riemann solvers. With $n \to \infty$, the erroneous mass flux either diverges or converges to a finite value. Table 7 shows the erroneous mass fluxes of different Riemann solvers when the number of time steps goes to infinity. It can be seen that only when all the perturbation errors in cell M are damped, i.e. the Riemann solver has both dissipation corresponding to entropy and shear waves (the pressure perturbation is always damped for these Godunov-type schemes), the mass flux can converge to a finite value and thus the instability can be suppressed. Otherwise, it diverges with the time-marching procedure. One should note that it is the linear analysis that leads to the erroneous mass flux going to infinity. The linear analysis doesn't hold after the error has grown beyond a point.
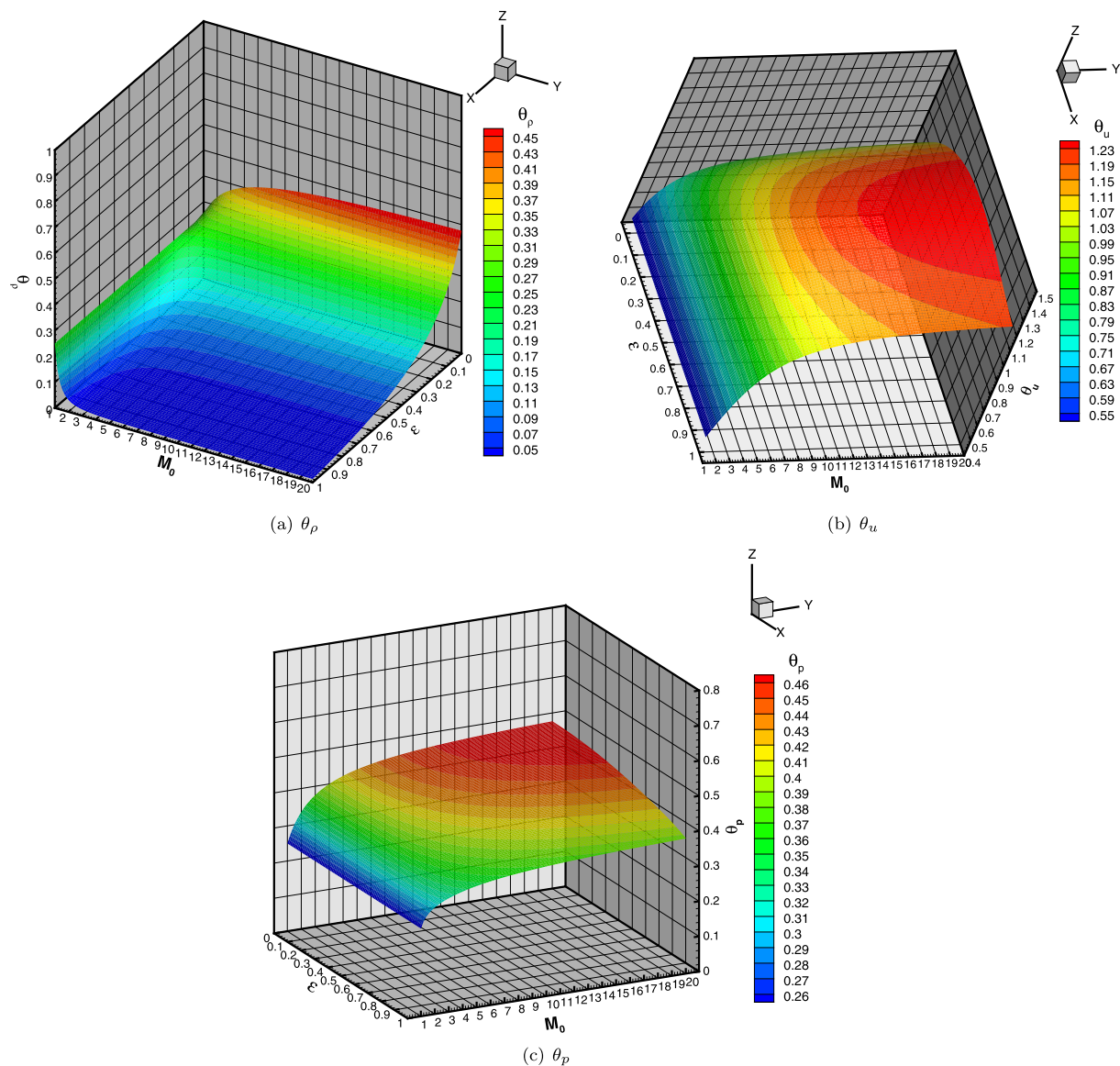
(a) θ_ρ

(b) θ_u

(c) θ_p

Fig. 9. Coefficients of the perturbation errors in (40) where the Courant number ν is 0.5. (For interpretation of the colors in this figure, the reader is referred to the web version of this article.)

Table 8
Summary of computed results of the HLLEM scheme for 1.5D steady shock problems ($M_0 = 6.0$, $\varepsilon = 0.3$; S: stable and converged, U: unstable; The red and blue interfaces shown in Fig. 11 are replaced by other Riemann solvers).

	HLLEM	HLLEC	HLLES	HLLE
Red interface	U	U	U	S
Blue interface	U	S	U	S

The above analysis indicates that there are two ways of suppressing the shock instability. One is damping all the perturbation errors inside the numerical shock structure and the other one is damping perturbed mass flux behind the shock. To further verify the results of the above analysis, we restart a series of 1.5D test cases on unstable shock positions in section 4.2. The basic scheme is still the HLLEM scheme, but the flux functions at the interfaces located inside the shock structure are replaced by the HLLEC scheme, the HLLES scheme and the HLLE scheme respectively, see Fig. 11 (the interfaces are flagged by red lines). These schemes will provide additional multidimensional dissipation to damp perturbation errors. The results of numerical experiments are summarized in Table 8. They show that only with the HLLE scheme applied, the
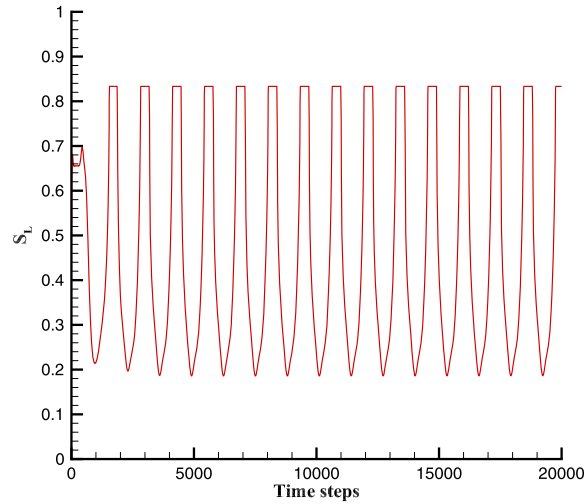
Fig. 10. Left wave speed estimate at the interface L, M for 1D shock instability case ($M_0 = 6.0$, $\varepsilon = 0.3$. Only the solutions before 20000 time steps are shown for clarity).
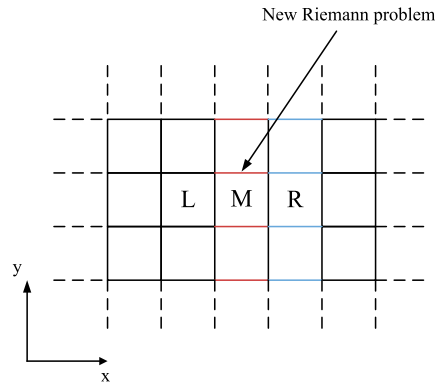

Fig. 11. Graphical illustration of the shock structure: L: left cells in the upstream region, M: intermediate cells inside the shock, R: right cells in the downstream region. The numerical fluxes applied at the interfaces denoted by black solid lines are always the HLLEM scheme, the numerical fluxes applied at the interfaces denoted by red and blue solid lines are replaced by HLLEC, HLLES and HLLE schemes respectively. (For interpretation of the references to color in this figure legend, the reader is referred to the web version of this article.)

shock instability can be successfully suppressed. It provides enough multidimensional dissipation to damp all the perturbation errors, but the others do not. This is in accordance with the results from the linearized perturbation analysis and it just further validates the conclusion 1 in section 4.3. Then a similar series of numerical tests is carried out with different Riemann solvers applied at interfaces just behind the shock, see Fig. 11 (the interfaces are flagged by blue lines). The results of numerical experiments are also summarized in Table 8. With the HLLEC and HLLE schemes applied at the interfaces behind the shock, the solutions are stable. In other words, only if the dissipation corresponding to the momentum is added behind the shock, the shock instability can be successfully suppressed. This validates the conclusion 2 in section 4.3 and supports the linearized perturbation analysis.

4.5. The explanation of the carbuncle phenomenon

Fig. 12 shows that the instability is developing at a certain time, the carbuncle phenomenon is characterized by several convex or concave wedge-shaped shock profiles distributed along the transversal direction in a staggered manner. By closely observing the flow field, we find that the mass flux behind the shock is much lower than that in front for a convex carbuncle and much higher for a concave one. Fig. 13 provides a schematic interpretation of the flow characteristics with the presence of the carbuncle. It can be speculated from the above perturbation analysis that the erroneous mass flux is a result of the amplifying effect of the initial perturbation errors inside the shock structure. For a convex carbuncle, physically, the flow controlled by the Euler equations will shunt redundant mass flux onto vertical direction, striving to maintain the consistency of mass flux across the shock. Because of extra mass flux in the vertical direction, the vertical velocity is never zero, the shock profile inevitably distorts. Numerically, this process is implemented by convections in the direction parallel to that of the shock front. When there are some perturbation errors being generated inside the shock structure, not only
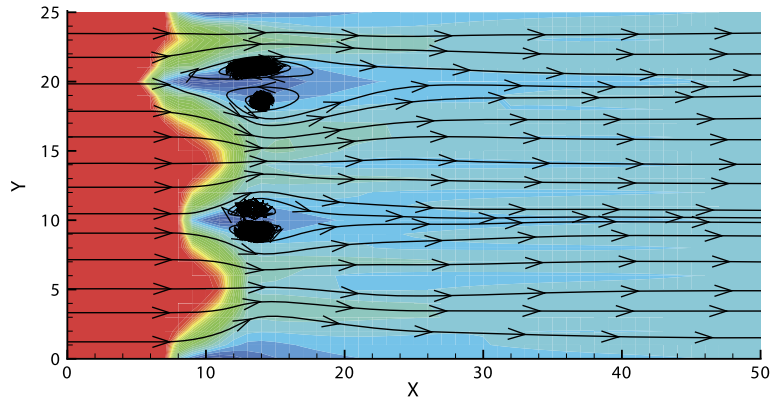
Fig. 12. Carbuncle: Mach number contours and streamlines at 1500 time steps ($M_0 = 6.0$, $\varepsilon = 0.3$).
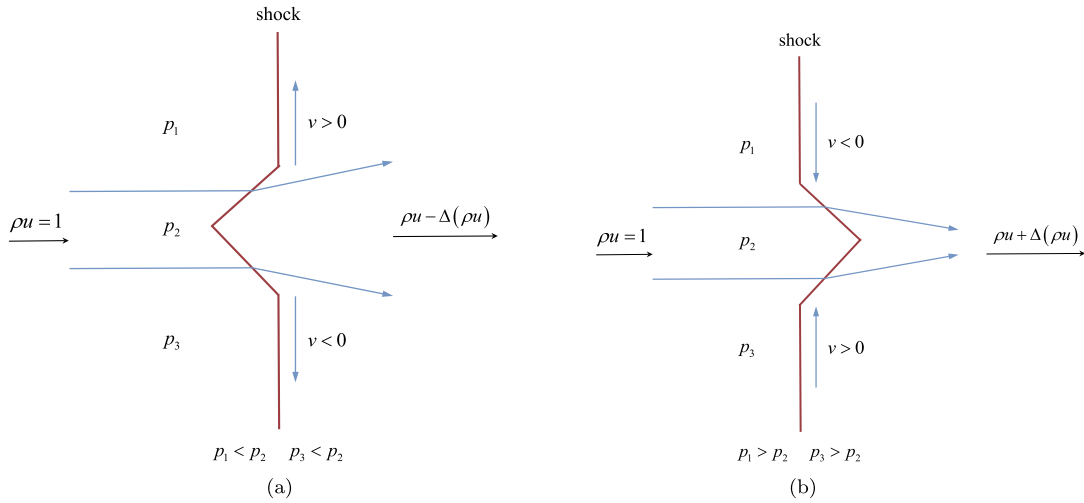

Fig. 13. Carbuncle schematic: (a) convex shock, (b) concave shock.

are these errors transported with entropy and acoustic waves along the *x*-direction, but they are also transported along the *y*-direction due to a new Riemann problem appearing at the interfaces perpendicular to the shock front (see Fig. 11). For a low diffusion Riemann solver, the dissipation is not enough to damp these perturbation errors effectively which further contaminate surrounding flow field except the upstream region of the shock. The concave carbuncle can be explained by a similar mechanism.

4.6. Discussion

The results of numerical experiments and the linearized perturbation analysis both support the viewpoint that the shock instability is strongly related to unstable behaviors of the intermediate states inside the numerical shock structure. Such a fact is predictable because there is no direct physical interpretation of the intermediate states. The shock wave is regarded as a jump discontinuity in terms of continuum mechanics on which the Euler equations are established. However, a physical shock wave has some finite width which is on the order of particle mean free path. To capture a shock, some additional amount of numerical dissipation inherent in approximate Riemann solvers must be introduced. With the explicit or implicit dissipation created artificially through the numerical procedure, a numerical shock can be obtained in the mesh size scale. However, in some circumstance, there is no guarantee that such artificial dissipation is always consistent with that required by the numerical shock structure, which is believed to be the underlying cause of the shock instability problem. A desirable Riemann solver should be carefully designed with proper artificial dissipation which is consistent with that required by the numerical shock. However, it is difficult to define what the proper dissipation is.

The 1.5D steady normal shock problem is set up to mimic a close-up view of a hypersonic flow ahead of a stagnation point of a two-dimensional blunt-body [27]. Hence, it largely predicts results of such flow computations at least in the stage where the blunt-body carbuncle develops. However, there is still a difference between them, the carbuncle solution of the blunt-body is steady and converged, which is not the case in the normal shock test. The blunt-body carbuncle appears to be a weak and consistent solution of the Euler equations, but not the physical one we desire. Numerical approximations
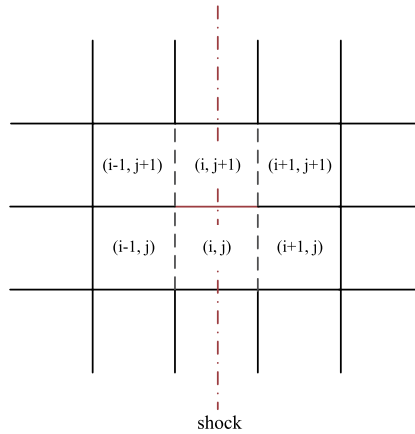
Fig. 14. Required interfaces to identify the cell interfaces for switching function. When calculating the flux on the interface denoted by the red solid line, the interfaces denoted by the dashed lines should be examined. (For interpretation of the references to color in this figure legend, the reader is referred to the web version of this article.)

for the Euler equations are usually not enforced with certain useful criterions such as the entropy condition for picking out the right solution among many converged weak solutions. The entropy condition is commonly used to guarantee that the entropy will increase across the shock, this helps the numerical approximations to recognize physical shocks while destabilizing rarefaction shocks. However, in most cases, numerical flux functions with the entropy condition enforced (e.g. the Roe scheme with Harten's entropy fix [35], the HLLEM scheme [29,4] and the Osher–Solomon scheme [31]) are still vulnerable to shock instability problems, particularly the carbuncle phenomenon. One should note that the entropy condition just guarantees that numerical approximations will produce the entropy in the right direction (i.e. the entropy will increase across the shock) but not necessarily in a right manner or in the right amounts. The numerical shock has several intermediate states, inappropriate production of entropy may happen inside the shock structure. How much entropy is needed to produce inside the shock structure and what is the proper entropy distribution within the shock structure? Such questions are closely tied to the artificial dissipation required by numerical methods to capture shocks stably and need to be explored further. Here, we mention the pioneer work of Ismail [39] and Ismail and Roe [34], who first investigate the effects of the entropy production on the shock stability. Their entropy-consistent flux [34] successfully eliminates the 1D shock instability through a proper entropy control even though it does not remove the multidimensional shock instability, particularly the carbuncle phenomenon. In the current study, we resort to a simple and effective way to remedy the multidimensional shock instability of low diffusion Riemann solvers, which will be the subject of the next section.

5. A shock-stable Godunov-type scheme

Through the shock instability analysis, it can be noticed that the shock instability can be cured by introducing numerical dissipation to make the mass flux consistent across the normal shock. This can be easily done in the framework of the unified Godunov-type schemes defined in (8) and Table 1. Around the strong shock, we just remove the anti-diffusion terms corresponding to shear waves, the HLLEM scheme then turns into the HLLEC scheme that accurately resolves contact waves but smears shear waves. The resulting flux function denoted as HLLEMS (i.e. **HLLEM** scheme with a **S**witching function) can be written as

$$\Phi_{\text{HLLEMS}} = \frac{S_R \mathbf{F}_n(\mathbf{U}_L) - S_L \mathbf{F}_n(\mathbf{U}_R)}{S_R - S_L} + \frac{S_L S_R}{S_R - S_L}(\mathbf{U}_R - \mathbf{U}_L - \delta_2 \widehat{\alpha}_2 \widehat{\mathbf{R}}_2 - f \delta_3 \widehat{\alpha}_3 \widehat{\mathbf{R}}_3) \tag{43}$$

In order to implement the switching between the HLLEM scheme and the HLLEC scheme, a pressure based weight function similar to that in [42] is defined as

$$f = min(f_{p,i-1/2,j}, f_{p,i-1/2,j+1}, f_{p,i+1/2,j}, f_{p,i+1/2,j+1})^3 \tag{44}$$

with

$$f_p = min(p_R/p_L, p_L/p_R) \tag{45}$$

where p_L and p_R are pressures which act on the cell interface. Fig. 14 shows the required interfaces for the function f. As shown in Fig. 14, when the numerical flux at the interface $(i, j + 1/2)$ is calculated (e.g. the interface denoted by a red solid line), the function f searches for the location where the shock discontinuity exists. Since the numerical dissipation is expected to be added at the interfaces normal to the shock, all the interfaces (e.g. the ones denoted by dotted lines) should be examined. In the vicinity of shock waves, the pressure difference is increased and the function f becomes very small, the flux function in (43) approaches the HLLEC scheme due to the diminishing anti-diffusion terms corresponding to

shear waves. In the smooth region, the pressure changes continuously and the pressure difference across the cell interface is small. The flux function in (43) approaches the HLLEM scheme which resolves contact and shear waves with minimal diffusion.

It should be noted that there are a variety of ways to choose the switching function such as the ones in [16,17]. A rotated approach [45] can also be used to implement hybridization of the HLLEM scheme and the HLLEC scheme in a single framework. The switching function can also be applied to the anti-diffusion terms corresponding to contact waves, then the flux function turns into the HLLE scheme in the vicinity of strong shocks just like other hybrid methods [2,16,17] have done. The analysis in the proceeding sections provides an in-depth explanation of why these hybrid methods [2,16,17] or the rotated method [45] can work well. These methods usually apply a dissipative scheme (e.g. the HLLE scheme [29] or the Rusanov scheme [37]) in the direction normal to shocks, the multidimensional dissipation of the scheme damps numerical perturbations generated inside the numerical shock structure and the mass flux perturbation just behind the shock. This helps to maintain the consistency of mass flux across the normal shock, so the shock stabilizes. However, it can be deduced from the analysis in the proceeding sections that the dissipation corresponding to shear waves can directly damp the mass flux perturbation effectively, thus it is enough to stabilize strong shocks. As a result, the flux function HLLEMS expressed in (43) can capture stationary contact waves exactly without the influence of the switching function. It has an advantage over some classical hybrid schemes, such as a hybridization of the HLLC scheme and the HLLE scheme or a combination between the Roe scheme and the HLLE scheme because the dissipation corresponding to contact waves are not influenced by the switching function. This is helpful to avoid the risk of introducing unnecessary numerical dissipation when the switching function does not work properly.

6. Numerical experiments

In this section, we will present numerical results of the HLLEMS scheme for other stringent shock wave problems as well as a boundary layer problem. The results computed by the HLLEMS scheme are compared with those of the HLLE scheme and the HLLEM scheme to show the improvements.

6.1. Quirk's odd–even grid perturbation problem

Quirk's odd–even decoupling test problem [2] consists of a single shock traveling from the left to the right at Mach 6. An 800×20 structured grid involving the following grid perturbations covers the domain:

$$y(i, j_{mid}) = \begin{cases} y_{mid} + 0.001 & \text{if } i \text{ is even} \\ y_{mid} - 0.001 & \text{if } i \text{ is odd} \end{cases} \tag{46}$$

where $y(i, j_{mid})$ is the y coordinate of a vertex $(i, 11)$, y_{mid} is the y coordinate of the halfway line. In order to trigger the instability more easily [46], the spacing in the y direction is shorten to be as half as that in the x direction. The domain has been initialized with $\rho = 1.4$, $p = 1.0$, $u = 0$ and $v = 0$. The inlet boundary condition is set to post shock values, nonreflecting simple wave boundary conditions are imposed at the outlet. The upper and lower boundaries are considered as solid walls. The CFL number is set to 0.5 for all the schemes to compute the solutions. Fig. 15 shows the contour plots of density at the time levels $t = 0$, $t = 25$ and $t = 50$, where there are 20 contour levels varying from 1.5 to 7.0.

As shown in Fig. 15, the shocks were destroyed by the HLLEM scheme and the HLLES scheme and typical carbuncles were developed. From the solutions of the HLLES scheme, it can be speculated that the dissipation corresponding to contact waves is helpful to suppress the odd–even decoupling, but it cannot remove it. The HLLEMS scheme preserved the initial shock successfully, just like the HLLE and HLLEC schemes did. The decoupling was completely eliminated. These three schemes all damp shear waves in the vicinity of shocks.

6.2. Hypersonic flow over a cylinder

Hypersonic flow over a blunt body is a typical problem to examine the catastrophic carbuncle failings of certain low diffusion upwind schemes. Such a phenomenon refers to a spurious bump on the bow shock near the flow center line ahead of the blunt body. The free stream Mach number is set as 20. A structured grid with 320 cells in the circumferential direction and 80 cells in the radial direction covers the computational domain.

Fig. 16 shows the density contours. As shown, the HLLEM and HLLES schemes created distorted solutions. Spurious bumps are clearly demonstrated by density contours near the stagnation streamline. The HLLEMS scheme along with the HLLE scheme and the HLLEC scheme produced a correct solution with a clean flow field behind the bow shock. In Fig. 17, the pressure profiles along the stagnation line for different schemes are plotted. As shown, the HLLEMS scheme produced an almost identical pressure profile as the HLLE and HLLEC schemes did.

6.3. Shock diffraction

This is another test case for which many low diffusion upwind schemes suffer from the carbuncle. The shock Mach number is 5.09. The computational domain is a unit square $[0, 1] \times [0, 1]$ covered by 400×400 uniform grids. The step is

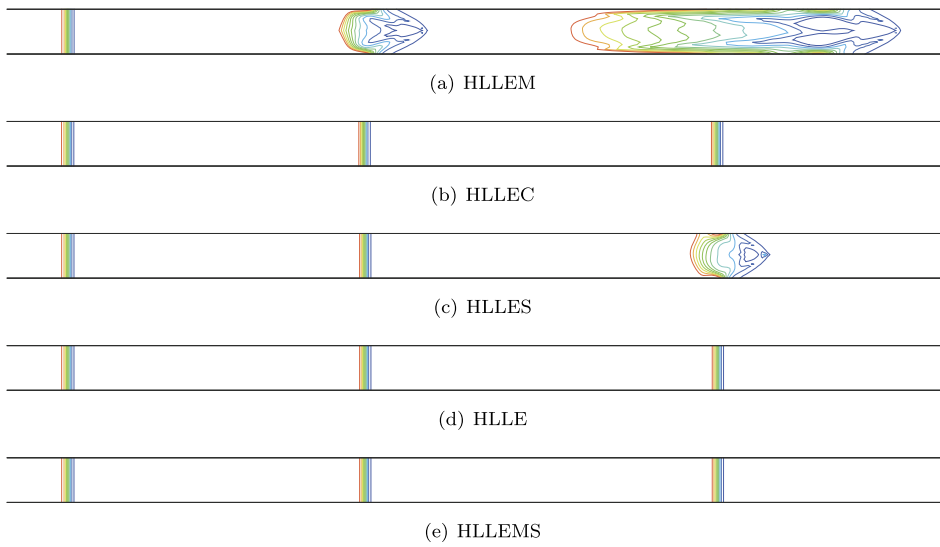(a) HLLEM

(b) HLLEC

(c) HLLES

(d) HLLE

(e) HLLEMS

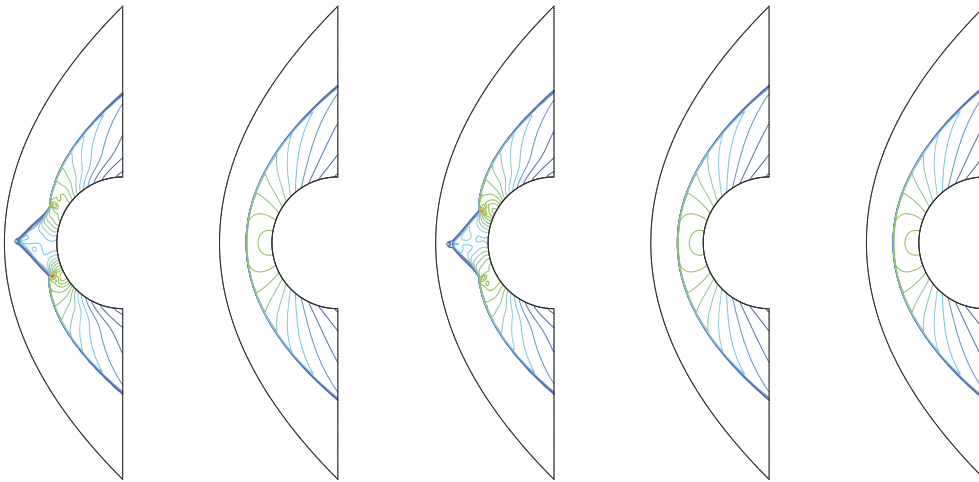**Fig. 15.** The density contours for the odd–even grid perturbation problem.

Fig. 16. The density contours for hypersonic flow over a cylinder. From left to right: HLLEM, HLLEC, HLLES, HLLE and HLLEMS.
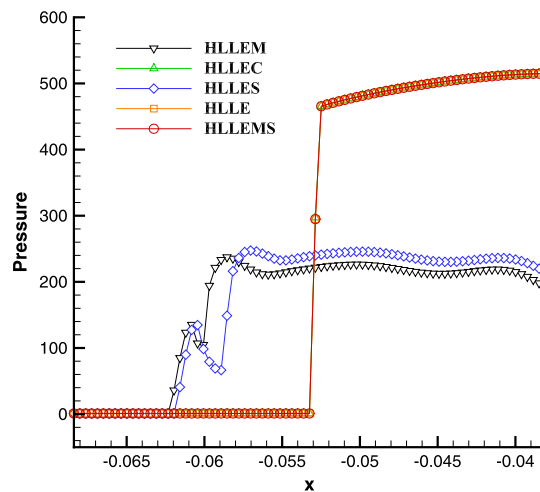

Fig. 17. The pressure profiles along the stagnation line for different schemes.
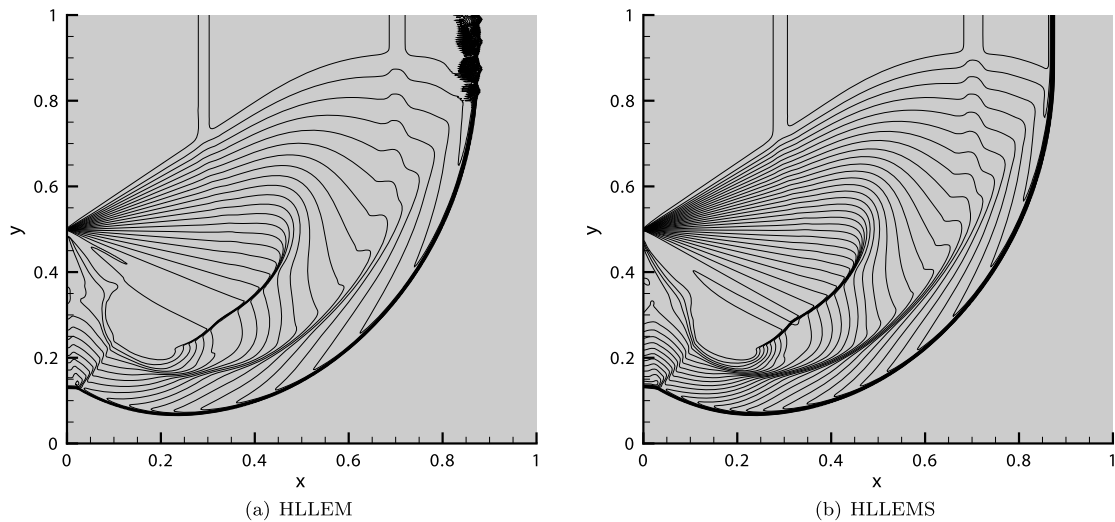
(a) HLLEM   (b) HLLEMS

Fig. 18. Shock diffraction: density contours at $t = 0.18$.

located at the midpoint of the left boundary: the lower half is treated as a wall; the top half is taken as an inflow [45]. The top boundary is set to a wall, and the right and bottom boundaries are taken as outflow. The solid walls are treated using the reflecting boundary conditions.

Fig. 18 shows the numerical results of the HLLEM scheme and the HLLEMS scheme in density contours. The HLLEM scheme does not show any problem at the corner, but spurious oscillations are explicitly observed at the planar moving shock. There are no shock instabilities in the results of the HLLEMS scheme. The secondary shock, contact surface, expansion wave and incident shock are well resolved by this scheme. The solutions of the HLLE, HLLEC and HLLES schemes are almost identical to that of the HLLEMS scheme, the contours are not shown for brevity.

6.4. Double Mach reflection problem

Many low diffusion upwind schemes have been reported to produce kinked Mach stem in double Mach reflection problem. Reference [47] gives the detailed information about the formulation of this problem, computational setup and discussion of the flow physics. The plots generated for $t = 0.2$ show complicated flow patterns containing two Mach shocks, two slip surfaces and a jet. The domain that is four unites long and one unit wide has been divided into 480 cells along the length and 120 cells along the width.

As shown in Fig. 19, the results of the HLLEM and HLLES schemes show explicit kinked Mach stems. However, the HLLEMS scheme and other shear dissipative schemes give clean shock fronts in the same area. This further demonstrates that the dissipation corresponding to shear waves is effective in suppressing the shock instability.

6.5. Flat plate boundary layer

The last case is the laminar boundary layer problem that is used to demonstrate the ability of the proposed scheme to resolve shear layer. The flow at $Ma = 0.3$ and $Re = 10^5$ over a flat plate is simulated using a second-order Navier–Stokes code. Fig. 20 shows the mesh with 120×30 non-uniform grid points. The computations were conducted for 50,000 steps with CFL $= 0.5$, and all the computations achieved at least three orders of magnitude reductions of the density residuals. The results of different schemes are compared in Fig. 21, as well as Blasius' analytical solution for a laminar boundary layer. As shown, the proposed scheme HLLEMS can successfully reproduce the analytical velocity profile just as the Roe scheme and the HLLEM scheme do. Actually, the results of these three solvers are almost identical. The HLLE scheme gives a very dissipative and inaccurate solution.

7. Conclusion

In this paper, we start by constructing a series of Godunov-type Riemann solvers with distinctive dissipative properties. With the help of both numerical experiments and a linearized analysis method, the instabilities of these Riemann solvers for strong shocks have been carefully examined. The results have shown that the numerical dissipation corresponding to shear waves are effective to stabilize the strong shock. The reason is that the dissipation corresponding to shear waves helps to maintain the consistency of mass flux across the normal shock by smearing perturbed momentum behind the shock. The consistency of mass flux across the normal shock is found to be the sufficient condition for Riemann solvers to capture strong shocks stably. The results of numerical experiments and the linearized analysis also clarify that the spatial source of
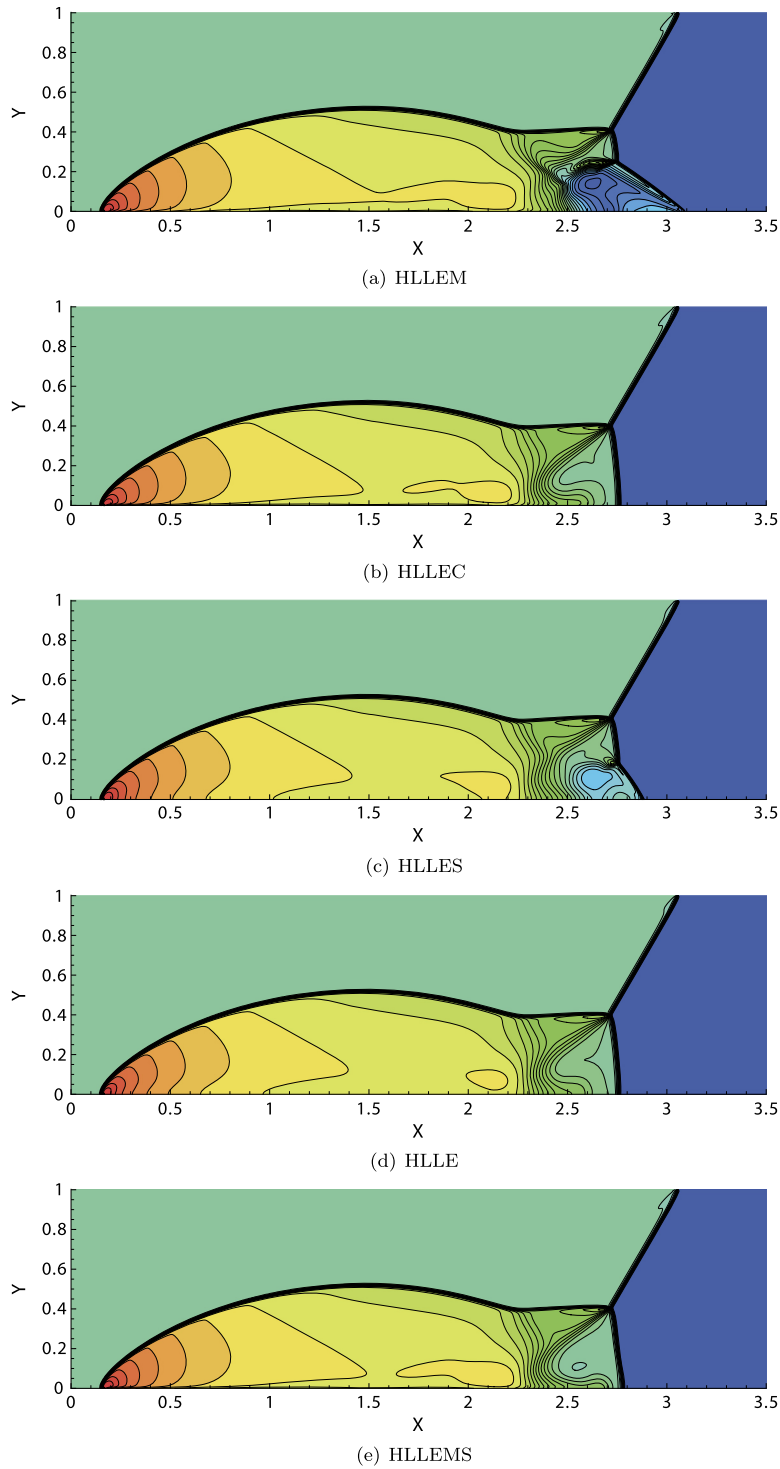
Fig. 19. Double Mach reflection: density contours at $t = 0.2$.

the instability lies inside the numerical shock structure which is deemed as unphysical. The famous carbuncle phenomenon is interpreted as the consequence of the inconsistency of mass flux across the normal shock for a low diffusion Riemann solver. A simple remedy for the shock instability is suggested for Godunov-type Riemann solvers by introducing additional dissipation corresponding to shear waves in the vicinity of strong shocks. Several carefully chosen stringent shock wave problems and a boundary layer problem have been tested to demonstrate its robustness and accuracy.
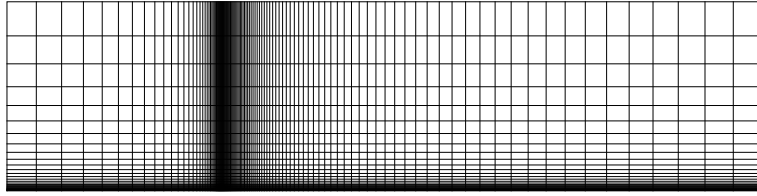
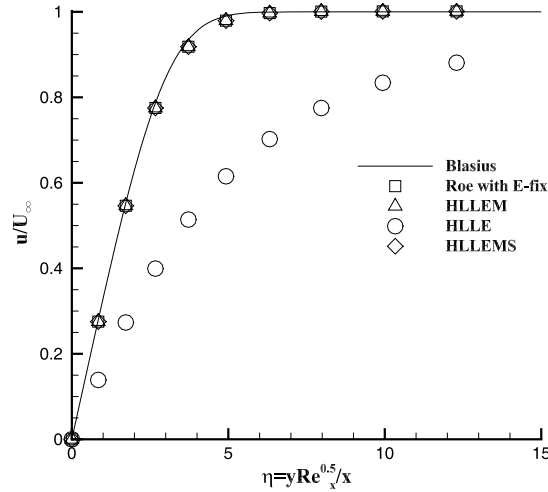**Fig. 20.** Mesh distribution for the laminar boundary layer computation (the minimal value of Δy is 0.05).

Fig. 21. Velocity profile for the flat plate boundary layer problem.

Acknowledgements

Appendix A

Here we provide the definitions of two modified Roe schemes presented in section 4.2. The original Roe scheme is often written in the following form:

$$\mathbf{\Phi}_{\text{Roe}} = \frac{1}{2} \left[\mathbf{F}_n \left(\mathbf{U}_L \right) + \mathbf{F}_n \left(\mathbf{U}_R \right) \right] - \frac{1}{2} \sum_{i=1}^{4} \widehat{\alpha}_i \left| \widehat{\lambda}_i \right| \widehat{\mathbf{R}}_i \tag{47}$$

where $\widehat{\alpha}_i$ and $\widehat{\mathbf{R}}_i$ are defined in Eqs. (10) and (11). To avoid non-physical expansion shocks, the moduli of the eigenvalues for the nonlinear fields $i = 1, 4$ can be modified by Harten's entropy fix [35] as follows:

$$\left| \overline{\lambda}_{1,4} \right| = \begin{cases} \left| \widehat{\lambda}_{1,4} \right| & \text{if } \left| \widehat{\lambda}_{1,4} \right| \geq \delta, \\ \frac{1}{2\delta} \left(\left| \widehat{\lambda}_{1,4} \right|^2 + \delta^2 \right) & \text{if } \left| \widehat{\lambda}_{1,4} \right| < \delta. \end{cases} \tag{48}$$

where $\delta = 0.2$.

To introduce the additional dissipation on linear waves, the Harten's entropy fix can be applied on the moduli of eigenvalues for the linear fields $i = 2, 3$ as follows:

$$\left| \overline{\lambda}_{2,3} \right| = \begin{cases} \left| \widehat{\lambda}_{2,3} \right| & \text{if } \left| \widehat{\lambda}_{2,3} \right| \geq \delta_*, \\ \frac{1}{2\delta_*} \left(\left| \widehat{\lambda}_{2,3} \right|^2 + \delta_*^2 \right) & \text{if } \left| \widehat{\lambda}_{2,3} \right| < \delta_*. \end{cases} \tag{49}$$

where the value of δ_* controls how much dissipation is introduced.

The modified Roe scheme with Harten's entropy fix on the moduli of all the eigenvalues can be written in the following form:

$$\Phi_{\text{Roe(E–fix)}} = \frac{1}{2} \left[\mathbf{F}_n \left(\mathbf{U}_L \right) + \mathbf{F}_n \left(\mathbf{U}_R \right) \right] - \frac{1}{2} \sum_{i=1}^{4} \widehat{\alpha}_i \left| \overline{\lambda}_i \right| \widehat{\mathbf{R}}_i \tag{50}$$

where $\left| \overline{\lambda}_i \right|$ are defined in Eqs. (48) and (49). To determine the value of δ_*, we carry out the analysis of the linearized form of the algorithms in section 3.3, the recursive formulas for the modified Roe schemes can be obtained as follows:

$$\delta \rho^{n+1} = \left(1 - \frac{2\nu}{\widehat{a}} \left| \overline{\lambda}_2 \right| \right) \cdot \delta \rho^n + \frac{2\nu}{\widehat{a}^2} \left(\frac{\left| \overline{\lambda}_2 \right|}{\widehat{a}} - 1 \right) \cdot \delta p^n$$
$$\delta u^{n+1} = \left(1 - \frac{2\nu}{\widehat{a}} \left| \overline{\lambda}_3 \right| \rho_0 \right) \cdot \delta u^n \tag{51}$$

It can be seen from the Eq. (51) that the $\left| \overline{\lambda}_2 \right|$ controls how the scheme damps the density perturbation and the $\left| \overline{\lambda}_3 \right|$ controls how the scheme damps the shear velocity perturbation. To make the modified Roe schemes damp the density perturbation and the shear velocity perturbation in the same way that the two-wave HLLE solver does, the values of $\left| \overline{\lambda}_i \right|$ can be obtained by comparison between equations in (51) and those of the HLLE scheme in Table 2 as follows:

$$\left| \overline{\lambda}_2 \right| = \left| \overline{\lambda}_3 \right| = \widehat{a} \tag{52}$$

Combining Eq. (49) and Eq. (52), the value of δ_* can be determined as follows:

$$\delta_* = 2\widehat{a} \tag{53}$$

The Roe (E-fix1) scheme is obtained by modifying the moduli of eigenvalues corresponding to the nonlinear waves and the entropy wave with Harten's entropy fix. It can be written as follows:

$$\Phi_{\text{Roe (E–fix1)}} = \frac{1}{2} \left[\mathbf{F}_n \left(\mathbf{U}_L \right) + \mathbf{F}_n \left(\mathbf{U}_R \right) \right] - \frac{1}{2} \widehat{\alpha}_1 \left| \overline{\lambda}_1 \right| \widehat{\mathbf{R}}_1 - \frac{1}{2} \widehat{\alpha}_2 \left| \overline{\lambda}_2 \right| \widehat{\mathbf{R}}_2 - \frac{1}{2} \widehat{\alpha}_3 \left| \widehat{\lambda}_3 \right| \widehat{\mathbf{R}}_3 - \frac{1}{2} \widehat{\alpha}_4 \left| \overline{\lambda}_4 \right| \widehat{\mathbf{R}}_4 \tag{54}$$

It's recursive formulas of the linear perturbations are written as follows:

$$\delta \rho^{n+1} = (1 - 2\nu) \cdot \delta \rho^n$$
$$\delta u^{n+1} = \delta u^n \tag{55}$$

Similarly, the Roe (E-fix2) scheme is obtained by modifying the moduli of eigenvalues corresponding to the nonlinear waves and the shear wave with Harten's entropy fix. It can be written as follows:

$$\Phi_{\text{Roe (E–fix2)}} = \frac{1}{2} \left[\mathbf{F}_n \left(\mathbf{U}_L \right) + \mathbf{F}_n \left(\mathbf{U}_R \right) \right] - \frac{1}{2} \widehat{\alpha}_1 \left| \overline{\lambda}_1 \right| \widehat{\mathbf{R}}_1 - \frac{1}{2} \widehat{\alpha}_2 \left| \widehat{\lambda}_2 \right| \widehat{\mathbf{R}}_2 - \frac{1}{2} \widehat{\alpha}_3 \left| \widehat{\lambda}_3 \right| \widehat{\mathbf{R}}_3 - \frac{1}{2} \widehat{\alpha}_4 \left| \overline{\lambda}_4 \right| \widehat{\mathbf{R}}_4 \tag{56}$$

It's recursive formulas of the linear perturbations are written as follows:

$$\delta \rho^{n+1} = \delta \rho^n - \frac{2\nu}{\widehat{a}^2} \cdot \delta p^n$$
$$\delta u^{n+1} = (1 - 2\nu \rho_0) \cdot \delta u^n \tag{57}$$

Appendix B

Here we give a detailed description of how to obtain the formulas presented in (39) and (40). At the time level t^n, it is assumed that there are some perturbations appearing in the cell M, the states in cells L and R remain unperturbed. These perturbation errors are assumed as follows:

$$\rho_M^n = \rho_M^{*,n} + \delta \rho_M^n, \quad (\rho u)_M^n = (\rho u)_M^{*,n} + \delta (\rho u)_M^n, \quad p_M^n = p_M^{*,n} + \delta p_M^n, \tag{58}$$

where $(\cdot)^*$ are the stable steady solutions, $\delta (\cdot)$ denote the perturbation errors that are the discrepancies between the perturbed states and the stable steady solutions. The conservative variables in cell R are

$$\rho_R^n = \rho_R^{*,n}, \quad (\rho u)_R^n = (\rho u)_R^{*,n}, \quad p_R^n = p_R^{*,n}. \tag{59}$$

The mass flux at the next time level can be updated through the integration of the second law of conservation (x-momentum) as

$$(\rho u)_R^{n+1} - (\rho u)_R^n = (\rho u)_R^{*,n+1} - (\rho u)_R^{*,n} + \delta (\rho u)_R^{n+1} - \delta (\rho u)_R^n$$
$$= \frac{\Delta t}{\Delta x} \left[\left(\rho u^2 + p \right)_{M,R}^n - \left(\rho u^2 + p \right)_{R,R'}^n \right] \tag{60}$$

where the flux function corresponding to the momentum component at the interface M, R can be written as

$$
\begin{aligned}
\left(\rho u^2 + p\right)^n_{M,R} &= \frac{S_R}{S_R - S_M}\left(\rho u^2 + p\right)^n_M - \frac{S_M}{S_R - S_M}\left(\rho u^2 + p\right)^n_R \\
&\quad + \frac{S_M S_R}{S_R - S_M}\left[(\rho u)^n_R - (\rho u)^n_M - \delta_2\left(\rho_R - \rho_M - \frac{p_R - p_M}{\widehat{a}^2}\right)\widehat{u}\right] \\
&= \frac{S_R}{S_R - S_M}\left\{\left[(\rho u)^{*,n}_M + \delta(\rho u)^n_M\right]\left(u^{*,n}_M + \delta u^n_M\right) + \left(p^{*,n}_M + \delta p^n_M\right)\right\} \\
&\quad - \frac{S_M}{S_R - S_M}\left[(\rho u)^*_R u^*_R + p^*_R\right] + \frac{S_M S_R}{S_R - S_M}\left\{(\rho u)^{*,n}_R - \left[(\rho u)^{*,n}_M + \delta(\rho u)^n_M\right]\right. \\
&\quad \left. - \delta_2\left(\rho^{*,n}_R - \rho^{*,n}_M - \delta\rho^n_M - \frac{p^{*,n}_R - p^{*,n}_M - \delta p^n_M}{\widehat{a}^2}\right)\widehat{u}\right\} \\
&= \frac{S_R}{S_R - S_M}\left[(\rho u)^{*,n}_M u^{*,n}_M + p^{*,n}_M\right] + \frac{S_R}{S_R - S_M}\left[(\rho u)^{*,n}_M \cdot \delta u^n_M + u^{*,n}_M \cdot \delta(\rho u)^n_M + \delta p^n_M\right] \\
&\quad - \frac{S_M}{S_R - S_M}\left[(\rho u)^*_R \cdot u^*_R + p^*_R\right] + \frac{S_M S_R}{S_R - S_M}\left[(\rho u)^*_R - (\rho u)^*_M - \delta_2\left(\rho^{*,n}_R - \rho^{*,n}_M\right.\right. \\
&\quad \left.\left. - \frac{p^{*,n}_R - p^{*,n}_M}{\widehat{a}^2}\right)\cdot\widehat{u}\right] - \frac{S_M S_R}{S_R - S_M}\left[\delta(\rho u)^n_M + \delta_2\cdot\left(-\delta\rho^n_M + \frac{\delta p^n_M}{\widehat{a}^2}\right)\cdot\widehat{u}\right] \\
&= \left(\rho u^2 + p\right)^{*,n}_{M,R} + \frac{S_R}{S_R - S_M}\left[(\rho u)^{*,n}_M \cdot \delta u^n_M + u^{*,n}_M \cdot \delta(\rho u)^n_M + \delta p^n_M\right] \\
&\quad - \frac{S_M S_R}{S_R - S_M}\left[\delta(\rho u)^n_M + \delta_2\cdot\left(-\delta\rho^n_M + \frac{\delta p^n_M}{\widehat{a}^2}\right)\cdot\widehat{u}\right] \\
&= \left(\rho u^2 + p\right)^{*,n}_{M,R} + \frac{S_R}{S_R - S_M}\left[(\rho u)^{*,n}_M \cdot \delta u^n_M + u^{*,n}_M \cdot \delta(\rho u)^n_M + \delta p^n_M\right. \\
&\quad \left. - S_M \cdot \delta(\rho u)^n_M + S_M \delta_2\cdot\left(\delta\rho^n_M - \frac{\delta p^n_M}{\widehat{a}^2}\right)\cdot\widehat{u}\right] \\
&= \left(\rho u^2 + p\right)^{*,n}_{M,R} + \frac{S_R}{S_R - S_M}\left[(\rho u)^{*,n}_M \cdot \delta u^n_M + \left(u^{*,n}_M\right)^2\delta\rho^n_M + (\rho u)^{*,n}_M \cdot \delta u^n_M\right. \\
&\quad \left. + \delta p^n_M - S_M u^{*,n}_M \cdot \delta\rho^n_M - S_M\rho^{*,n}_M \cdot \delta u^n_M + S_M\delta_2\widehat{u}\cdot\delta\rho^n_M - \frac{S_M\delta_2\widehat{u}}{\widehat{a}^2}\delta p^n_M\right] \\
&= \left(\rho u^2 + p\right)^{*,n}_{M,R} + \frac{S_R}{S_R - S_M}\left\{\left[2(\rho u)^{*,n}_M - S_M\rho^{*,n}_M\right]\cdot\delta u^n_M\right. \\
&\quad \left. + \left[\left(u^{*,n}_M\right)^2 - S_M u^{*,n}_M + S_M\delta_2\widehat{u}\right]\cdot\delta\rho^n_M + \left[1 - \frac{S_M\delta_2\widehat{u}}{\widehat{a}^2}\right]\cdot\delta p^n_M\right\}
\end{aligned}
\tag{61}
$$

The flux function corresponding to the momentum component at the interface R, R' can be written as

$$
\left(\rho u^2 + p\right)^n_{R,R'} = \left(\rho u^2 + p\right)^{*,n}_R
\tag{62}
$$

Inserting Eqs. (61) and (62) into Eq. (60), it can be obtained that

$$
\begin{aligned}
(\rho u)^{n+1}_R - (\rho u)^n_R &= (\rho u)^{*,n+1}_R - (\rho u)^{*,n}_R + \delta(\rho u)^{n+1}_R - \delta(\rho u)^n_R \\
&= \frac{\Delta t}{\Delta x}\left[\left(\rho u^2 + p\right)^n_{M,R} - \left(\rho u^2 + p\right)^n_{R,R'}\right] \\
&= \frac{\Delta t}{\Delta x}\left\{\left(\rho u^2 + p\right)^{*,n}_{M,R} - \left(\rho u^2 + p\right)^{*,n}_R + \frac{S_R}{S_R - S_M}\left\{\left[2(\rho u)^{*,n}_M - S_M\rho^{*,n}_M\right]\cdot\delta u^n_M\right.\right. \\
&\quad \left.\left. + \left[\left(u^{*,n}_M\right)^2 - S_M u^{*,n}_M + S_M\delta_2\widehat{u}\right]\cdot\delta\rho^n_M + \left[1 - \frac{S_M\delta_2\widehat{u}}{\widehat{a}^2}\right]\cdot\delta p^n_M\right\}\right\}
\end{aligned}
\tag{63}
$$

It should be noted that

$$
(\rho u)^{*,n+1}_R - (\rho u)^{*,n}_R = \frac{\Delta t}{\Delta x}\left[\left(\rho u^2 + p\right)^{*,n}_{M,R} - \left(\rho u^2 + p\right)^{*,n}_R\right]
\tag{64}
$$

Subtracting Eq. (64) from Eq. (63), it can be obtained that

$$
\begin{aligned}
\delta \left(\rho u\right)_R^{n+1} - \delta \left(\rho u\right)_R^n = \frac{\Delta t}{\Delta x} \frac{S_R}{S_R - S_M} &\left\{ \left[2 \left(\rho u\right)_M^{*,n} - S_M \rho_M^{*,n}\right] \cdot \delta u_M^n + \left[\left(u_M^{*,n}\right)^2 - S_M u_M^{*,n} + S_M \delta_2 \widehat{u}\right] \cdot \delta \rho_M^n \right. \\
&\left. + \left[1 - \frac{S_M \delta_2 \widehat{u}}{\widehat{a}^2}\right] \cdot \delta p_M^n \right\}
\end{aligned}
\tag{65}
$$

At time t^n, it is assumed that the stable steady states $(\cdot)^*$ inside the cell M have the following relationship with those in cell L and cell R.

$$
\begin{aligned}
\rho_M^{*,n} &= \left(1 - \alpha_\rho\right) \rho_L^{*,n} + \alpha_\rho \rho_R^{*,n} \\
u_M^{*,n} &= (1 - \alpha_u) u_L^{*,n} + \alpha_u u_R^{*,n} \\
p_M^{*,n} &= \left(1 - \alpha_p\right) p_L^{*,n} + \alpha_p p_R^{*,n}
\end{aligned}
\tag{66}
$$

From the initial conditions in Eqs. (29), we can obtain

$$
\begin{aligned}
\rho_R^{*,n} &= f \cdot \rho_L^{*,n} \\
u_R^{*,n} &= \frac{1}{f} \cdot u_L^{*,n} \\
p_R^{*,n} &= g \cdot p_L^{*,n}
\end{aligned}
\tag{67}
$$

Combining Eqs. (66) and Eqs. (67), it can be obtained that

$$
\begin{aligned}
\rho_M^{*,n} &= \frac{1 - \alpha_\rho + f \cdot \alpha_\rho}{f} \rho_R^{*,n} \\
u_M^{*,n} &= (f - f \cdot \alpha_u + \alpha_u) \cdot u_R^{*,n} \\
p_M^{*,n} &= \frac{1 - \alpha_p + g \cdot \alpha_p}{g} p_R^{*,n}
\end{aligned}
\tag{68}
$$

For convenience, three coefficients σ, ω and ψ are defined as follows:

$$
\begin{aligned}
\sigma &= \frac{1 - \alpha_\rho + f \cdot \alpha_\rho}{f} \\
\omega &= f - f \cdot \alpha_u + \alpha_u \\
\psi &= \frac{1 - \alpha_p + g \cdot \alpha_p}{g}
\end{aligned}
\tag{69}
$$

where the definitions of these parameters α_ρ, α_u and α_p can refer to Eqs. (32).

Inserting Eqs. (68) and Eqs. (69) into Eq. (65), the Eq. (65) can be further simplified as

$$
\begin{aligned}
\delta \left(\rho u\right)_R^{n+1} - \delta \left(\rho u\right)_R^n = \frac{\Delta t}{\Delta x} \frac{S_R}{S_R - S_M} &\left\{ \left(2\sigma\omega \cdot \rho_R^{*,n} u_R^{*,n} - S_M \sigma \cdot \rho_R^{*,n}\right) \cdot \delta u_M^n \right. \\
&\left. + \left[\omega^2 \cdot \left(u_R^{*,n}\right)^2 - S_M \omega \cdot u_R^{*,n} + S_M \delta_2 \widehat{u}\right] \cdot \delta \rho_M^n + \left(1 - \frac{S_M \cdot \delta_2 \cdot \widehat{u}}{\widehat{a}^2}\right) \cdot \delta p_M^n \right\}
\end{aligned}
\tag{70}
$$

The Roe's averaged velocity $\widehat{u}$ can be approximated as

$$
r = \sqrt{\frac{\rho_R^n}{\rho_M^n}} = \sqrt{\frac{\rho_R^{*,n}}{\rho_M^{*,n} + \delta \rho_M^n}} \approx \frac{1}{\sqrt{\sigma}}
\tag{71}
$$

$$
\widehat{u} = \frac{u_M^n + r \cdot u_R^n}{1 + r} = \frac{u_M^{*,n} + r \cdot u_R^{*,n} + \delta u_M^n}{1 + r} = \widehat{u}^* + \frac{\delta u_M^n}{1 + r} = \widehat{u}^* + \frac{\sqrt{\sigma}}{\sqrt{\sigma} + 1} \cdot \delta u_M^n
\tag{72}
$$

Refer to the problem described in Section 4.1 and to the relative definitions given there, we obtain

$$
\rho_R^{*,n} u_R^{*,n} = 1, \qquad u_R^{*,n} = \frac{1}{f} \cdot u_L^{*,n} = \frac{1}{f} \qquad \rho_R^{*,n} = f \cdot \rho_L^{*,n} = f.
\tag{73}
$$

Inserting Eqs. (72) and (73) into Eq. (70), we obtain

$$\delta \left(\rho u\right)_R^{n+1} - \delta \left(\rho u\right)_R^n = \frac{\Delta t}{\Delta x} \frac{S_R}{S_R - S_M} \left[\left(\frac{\omega^2}{f^2} - \frac{S_M \omega}{f} + \frac{S_M \delta_2}{f} \frac{1 + \omega \sqrt{\sigma}}{1 + \sqrt{\sigma}} \right) \cdot \delta \rho_M^n \right.$$
$$\left. + \left(2 \sigma \omega - S_M \sigma f\right) \cdot \delta u_M^n + \left(1 - \frac{S_M \delta_2}{\widehat{a}^2 f} \frac{1 + \sqrt{\sigma} \omega}{1 + \sqrt{\sigma}} \right) \cdot \delta p_M^n \right] \tag{74}$$

The term $\frac{\Delta t}{\Delta x}$ can be approximated as

$$\frac{\Delta t}{\Delta x} \approx \frac{\nu \Delta x}{(|u| + a)_{\max} \Delta x} = \frac{\nu}{u_0 + a_0} = \frac{\nu M_0}{1 + M_0} \tag{75}$$

where ν is the Courant number, u_0 and a_0 are the velocity and the speed of sound in the upstream region, M_0 is the freestream Mach number. Inserting the Eq. (75) into Eq. (74), it can be obtained that

$$\delta \left(\rho u\right)_R^{n+1} - \delta \left(\rho u\right)_R^n = \theta_\rho \cdot \delta \rho_M^n + \theta_u \cdot \delta u_M^n + \theta_p \cdot \delta p_M^n \tag{76}$$

with

$$\theta_\rho = \frac{S_R \nu M_0}{(S_R - S_M)(1 + M_0)} \left(\frac{\omega^2}{f^2} - \frac{S_M \omega}{f} + \frac{S_M \delta_2}{f} \frac{1 + \omega \sqrt{\sigma}}{1 + \sqrt{\sigma}} \right)$$
$$\theta_u = \frac{S_R \nu M_0}{(S_R - S_M)(1 + M_0)} \left(2 \sigma \omega - S_M \sigma f\right) \tag{77}$$
$$\theta_p = \frac{S_R \nu M_0}{(S_R - S_M)(1 + M_0)} \left(1 - \frac{S_M \delta_2}{\widehat{a}^2 f} \frac{1 + \sqrt{\sigma} \omega}{1 + \sqrt{\sigma}} \right)$$

Appendix C

Here we give a detailed description of how to obtain the formulas presented in (42). The recursive formulas of perturbed quantities in cell M for Godunov-type Riemann solvers can be written in a unified form as

$$\delta \rho^{n+1} = a_1 \cdot \delta \rho^n + a_2 \cdot \delta p^n$$
$$\delta u^{n+1} = a_3 \cdot \delta u^n \tag{78}$$
$$\delta p^{n+1} = a_4 \cdot \delta p^n$$

where some symbols are introduced for convenience to denote the coefficients as

$$a_1 = 1 - 2\nu \left(1 - \delta_2\right),$$
$$a_2 = -\frac{2\nu}{\widehat{a}^2} \delta_2,$$
$$a_3 = 1 - 2\nu \cdot \rho_0 \cdot \left(1 - \delta_3\right), \tag{79}$$
$$a_4 = 1 - 2\nu.$$

where ν is the Courant number.

The perturbed mass flux in cell R at time level t^n can be obtained by a cumulative calculation of Eq. (76) as

$$\delta(\rho u)_R^n - \delta(\rho u)_R^0 = \delta(\rho u)_R^n - \delta(\rho u)_R^{n-1} + \delta(\rho u)_R^{n-1} - \delta(\rho u)_R^{n-2} + \dots + \delta(\rho u)_R^1 - \delta(\rho u)_R^0$$
$$= \theta_\rho \cdot \delta \rho^{n-1} + \theta_u \cdot \delta u^{n-1} + \theta_p \cdot \delta p^{n-1} + \theta_\rho \cdot \delta \rho^{n-2} + \theta_u \cdot \delta u^{n-2} + \theta_p \cdot \delta p^{n-2}$$
$$+ \dots + \theta_\rho \cdot \delta \rho^0 + \theta_u \cdot \delta u^0 + \theta_p \cdot \delta p^0 \tag{80}$$
$$= \theta_\rho \cdot \left(\delta \rho^0 + \delta \rho^1 + \dots + \delta \rho^{n-1}\right) + \theta_u \cdot \left(\delta u^0 + \delta u^1 + \dots + \delta u^{n-1}\right)$$
$$+ \theta_p \cdot \left(\delta p^0 + \delta p^1 + \dots + \delta p^{n-1}\right)$$

with the coefficients θ_ρ, θ_u and θ_p defined in Eqs. (77). In Eq. (80), the subscript M has been omitted for clarity.

The sums of these progressions of perturbed quantities in (80) can be evaluated as

$$\delta u^0 + \delta u^1 + \dots + \delta u^{n-1} = \delta u^0 + a_3 \cdot \delta u^0 + \dots + a_3^{n-1} \cdot \delta u^0$$
$$= \begin{cases} \frac{1 - a_3^n}{1 - a_3} \cdot \delta u^0 & |a_3| < 1, \\ n \cdot \delta u^0 & |a_3| = 1. \end{cases} \tag{81}$$

Under the situation $|a_1| < 1$, the sum of the progression of perturbed density can be evaluated as

$$
\begin{aligned}
\delta\rho^0 + \delta\rho^1 + \cdots + \delta\rho^{n-1} &= \delta\rho^0 + a_1\left(\delta\rho^0 + \delta\rho^1 + \cdots + \delta\rho^{n-2}\right) + a_2\left(\delta p^0 + \delta p^1 + \cdots + \delta p^{n-2}\right) \\
&= \left(1 + a_1 + \ldots + a_1^{n-1}\right)\delta\rho^0 + a_2\left(1 + a_1 + \ldots + a_1^{n-2}\right)\delta p^0 \\
&\quad + a_2\left(1 + a_1 + \ldots + a_1^{n-3}\right)\delta p^1 + \ldots + a_2\delta p^{n-2} \\
&= \frac{1-a_1^n}{1-a_1}\delta\rho^0 + a_2\frac{1-a_1^{n-1}}{1-a_1}\delta p^0 + a_2\frac{1-a_1^{n-2}}{1-a_1}\delta p^1 + \ldots + a_2\frac{1-a_1}{1-a_1}\delta p^{n-2} \\
&= \frac{1-a_1^n}{1-a_1}\delta\rho^0 + \frac{a_2}{1-a_1}\left(\delta p^0 + \delta p^1 + \ldots + \delta p^{n-2}\right) \\
&\quad - \frac{a_2}{1-a_1}\left(a_1^{n-1}\delta p^0 + a_1^{n-2}\delta p^1 + \ldots + a_1\delta p^{n-2}\right) \\
&= \frac{1-a_1^n}{1-a_1}\delta\rho^0 + \frac{a_2}{1-a_1}\cdot\frac{1-a_4^{n-1}}{1-a_4}\delta p^0 - \frac{a_2}{1-a_1}\cdot\frac{a_1^n - a_1 a_4^{n-1}}{a_1 - a_4}\delta p^0 \\
&= \frac{1-a_1^n}{1-a_1}\delta\rho^0 + \frac{a_2}{1-a_1}\cdot\left(\frac{1-a_4^{n-1}}{1-a_4} - \frac{a_1^n - a_1 a_4^{n-1}}{a_1 - a_4}\right)\delta p^0
\end{aligned}
\tag{82}
$$

For the case $|a_1| = 1$, one obtains

$$
\begin{aligned}
\delta\rho^0 + \delta\rho^1 + \cdots + \delta\rho^{n-1} &= \delta\rho^0 + a_1\left(\delta\rho^0 + \delta\rho^1 + \cdots + \delta\rho^{n-2}\right) + a_2\left(\delta p^0 + \delta p^1 + \cdots + \delta p^{n-2}\right) \\
&= \left(1 + a_1 + a_1^2 + \ldots + a_1^{n-1}\right)\delta\rho^0 + a_2\left(1 + a_1 + \ldots + a_1^{n-2}\right)\delta p^0 \\
&\quad + a_2\left(1 + a_1 + \ldots + a_1^{n-3}\right)\delta p^1 + \ldots + a_2\delta p^{n-2} \\
&= n\delta\rho^0 + a_2(n-1)\delta p^0 + a_2(n-2)\delta p^1 + \ldots + a_2[n-(n-1)]\delta p^{n-2} \\
&= n\delta\rho^0 + a_2 n\left(\delta p^0 + \delta p^1 + \ldots + \delta p^{n-2}\right) \\
&\quad - a_2\left[\delta p^0 + 2\delta p^1 + \ldots + (n-1)\delta p^{n-2}\right] \\
&= n\delta\rho^0 + a_2 n\frac{1-a_4^{n-1}}{1-a_4}\delta p^0 - \frac{a_2}{1-a_4}\left[\frac{1-a_4^{n-1}}{1-a_4} - (n-1)a_4^{n-1}\right]\delta p^0 \\
&= n\delta\rho^0 + a_2 n\frac{1-a_4^{n-1}}{1-a_4}\delta p^0 - \frac{a_2}{(1-a_4)^2}\left[1 - na_4^{n-1} + (n-1)a_4^n\right]\delta p^0 \\
&= n\delta\rho^0 + \frac{a_2}{(1-a_4)^2}\left(n - na_4 - 1 + a_4^n\right)\delta p^0
\end{aligned}
\tag{83}
$$

$$
\begin{aligned}
\delta p^0 + \delta p^1 + \cdots + \delta p^{n-1} &= \delta p^0 + a_4 \cdot \delta p^0 + \ldots + a_4^{n-1}\cdot\delta p^0 \\
&= \frac{1-a_4^n}{1-a_4}\cdot\delta p^0
\end{aligned}
\tag{84}
$$

Inserting these Eqs. (81)∼(84) into (80), we will obtain

$$
\delta(\rho u)_R^n - \delta(\rho u)_R^0 = \alpha \cdot \delta\rho_M^0 + \beta \cdot \delta u_M^0 + \gamma \cdot \delta p_M^0
\tag{85}
$$

where the coefficients α, β and γ are determined as follows:

For the HLLEM scheme, there are $|a_1| = 1$ and $|a_3| = 1$, we will obtain

$$
\begin{aligned}
\alpha &= \frac{S_R \nu M_0}{(S_R - S_M)(1+M_0)}\left(\frac{\omega^2}{f^2} - \frac{S_M\omega}{f} + \frac{S_M\delta_2}{f}\frac{1+\omega\sqrt{\sigma}}{1+\sqrt{\sigma}}\right)\cdot n, \\
\beta &= \frac{S_R \nu M_0}{(S_R - S_M)(1+M_0)}\left(2\sigma\omega - S_M\sigma f\right)\cdot n, \\
\gamma &= \frac{S_R \nu M_0}{(S_R - S_M)(1+M_0)}\left(\frac{\omega^2}{f^2} - \frac{S_M\omega}{f} + \frac{S_M\delta_2}{f}\frac{1+\omega\sqrt{\sigma}}{1+\sqrt{\sigma}}\right)\cdot\frac{1-2n\nu-(1-2\nu)^n}{2\widehat{a}^2\nu} \\
&\quad + \frac{S_R \nu M_0}{(S_R - S_M)(1+M_0)}\left(1 - \frac{S_M\delta_2}{\widehat{a}^2 f}\frac{1+\omega\sqrt{\sigma}}{1+\sqrt{\sigma}}\right)\cdot\frac{1-(1-2\nu)^n}{2\nu}.
\end{aligned}
\tag{86}
$$

Inserting Eq. (86) into Eq. (85), it can be obtained that $\delta(\rho u)^\infty = \infty$ as $n \to \infty$.

For the HLLEC scheme, there are $|a_1| = 1$ and $|a_3| < 1$, the coefficient δ_3 is equal to zero, we will obtain

$$
\begin{aligned}
\alpha &= \frac{S_R \nu M_0}{(S_R - S_M)(1 + M_0)} \left(\frac{\omega^2}{f^2} - \frac{S_M \omega}{f} + \frac{S_M \delta_2}{f} \frac{1 + \omega \sqrt{\sigma}}{1 + \sqrt{\sigma}} \right) \cdot n, \\
\beta &= \frac{S_R \nu M_0}{(S_R - S_M)(1 + M_0)} (2\sigma\omega - S_M \sigma f) \cdot \frac{1 - (1 - 2\nu)^n}{2\nu}, \\
\gamma &= \frac{S_R \nu M_0}{(S_R - S_M)(1 + M_0)} \left(\frac{\omega^2}{f^2} - \frac{S_M \omega}{f} + \frac{S_M \delta_2}{f} \frac{1 + \omega \sqrt{\sigma}}{1 + \sqrt{\sigma}} \right) \cdot \frac{1 - n\nu - (1 - 2\nu)^n}{2\widehat{a}^2 \nu} \\
&\quad + \frac{S_R \nu M_0}{(S_R - S_M)(1 + M_0)} \left(1 - \frac{S_M \delta_2}{\widehat{a}^2 f} \frac{1 + \omega \sqrt{\sigma}}{1 + \sqrt{\sigma}} \right) \cdot \frac{1 - (1 - 2\nu)^n}{2\nu}.
\end{aligned}
\tag{87}
$$

Inserting Eq. (87) into Eq. (85), it can be obtained that $\delta(\rho u)^\infty = \infty$ as $n \to \infty$.

For the HLLES scheme, there are $|a_1| < 1$ and $|a_3| = 1$, the coefficient δ_2 is equals to zero, we will obtain

$$
\begin{aligned}
\alpha &= \frac{S_R \nu M_0}{(S_R - S_M)(1 + M_0)} \left(\frac{\omega^2}{f^2} - \frac{S_M \omega}{f} \right) \cdot \frac{1 - (1 - 2\nu)^n}{2\nu}, \\
\beta &= \frac{S_R \nu M_0}{(S_R - S_M)(1 + M_0)} (2\sigma\omega - S_M \sigma f) \cdot n, \\
\gamma &= \frac{S_R \nu M_0}{(S_R - S_M)(1 + M_0)} \cdot \frac{1 - (1 - 2\nu)^n}{2\nu}.
\end{aligned}
\tag{88}
$$

Inserting Eq. (88) into Eq. (85), it can be obtained that $\delta(\rho u)^\infty = \infty$ as $n \to \infty$.

Finally, for the HLLE scheme, there are $|a_1| < 1$ and $|a_3| < 1$, the coefficients δ_2 and δ_3 are equal to zero, we will obtain

$$
\begin{aligned}
\alpha &= \frac{S_R \nu M_0}{(S_R - S_M)(1 + M_0)} \left(\frac{\omega^2}{f^2} - \frac{S_M \omega}{f} \right) \cdot \frac{1 - (1 - 2\nu)^n}{2\nu}, \\
\beta &= \frac{S_R \nu M_0}{(S_R - S_M)(1 + M_0)} (2\sigma\omega - S_M \sigma f) \cdot \frac{1 - (1 - 2\nu)^n}{2\nu}, \\
\gamma &= \frac{S_R \nu M_0}{(S_R - S_M)(1 + M_0)} \cdot \frac{1 - (1 - 2\nu)^n}{2\nu}.
\end{aligned}
\tag{89}
$$

Inserting Eq. (89) into Eq. (85), we can obtain the following equation as

$$
\delta(\rho u)_R^\infty = \delta(\rho u)_R^0 + \frac{S_R M_0}{2(S_R - S_M)(1 + M_0)} \left[\left(\frac{\omega^2}{f^2} - \frac{S_M \omega}{f} \right) \cdot \delta \rho_M^0 + (2\sigma\omega - S_M \sigma f) \cdot \delta u_M^0 + \delta p_M^0 \right].
\tag{90}
$$

References

[1] P. Roe, H. Nishikawa, F. Ismail, L. Scalabrin, On carbuncles and other excrescences, in: 17th AIAA Computational Fluid Dynamics Conference, 2005, p. 4872.
[2] J.J. Quirk, A contribution to the great Riemann solver debate, Int. J. Numer. Methods Fluids 18 (6) (1994) 555–574.
[3] M. Pandolfi, D. D'Ambrosio, Numerical instabilities in upwind methods: analysis and cures for the "carbuncle" phenomenon, J. Comput. Phys. 166 (2) (2001) 271–301.
[4] B. Einfeldt, C.-D. Munz, P.L. Roe, B. Sjögreen, On Godunov-type methods near low densities, J. Comput. Phys. 92 (2) (1991) 273–295.
[5] B. van Leer, Flux-vector splitting for the Euler equations, in: Eighth International Conference on Numerical Methods in Fluid Dynamics, Springer, 1982, pp. 507–512.
[6] J. Gressier, J.-M. Moschetta, Robustness versus accuracy in shock-wave computations, Int. J. Numer. Methods Fluids 33 (3) (2000) 313–332.
[7] J. Mandal, V. Panwar, Robust HLL-type Riemann solver capable of resolving contact discontinuity, Comput. Fluids 63 (2012) 148–164.
[8] Z. Shen, W. Yan, G. Yuan, A robust HLLC-type Riemann solver for strong shock, J. Comput. Phys. 309 (2016) 185–206.
[9] M. Sun, K. Takayama, An artificially upstream flux vector splitting scheme for the Euler equations, J. Comput. Phys. 189 (1) (2003) 305–329.
[10] W. Xie, H. Li, Z. Tian, S. Pan, A low diffusion flux splitting method for inviscid compressible flows, Comput. Fluids 112 (2015) 83–93.
[11] W. Xie, H. Li, Z. Tian, S. Pan, On the accuracy and robustness of a new flux splitting method, Acta Phys. Sin. 64 (2) (2015) 024702.
[12] R. Sanders, E. Morano, M.-C. Druguet, Multidimensional dissipation for upwind schemes: stability and applications to gas dynamics, J. Comput. Phys. 145 (2) (1998) 511–537.
[13] Z. Shen, W. Yan, G. Yuan, A stability analysis of hybrid schemes to cure shock instability, Commun. Comput. Phys. 15 (05) (2014) 1320–1342.
[14] M.-S. Liou, Mass flux schemes and connection to shock instability, J. Comput. Phys. 160 (2) (2000) 623–648.
[15] S.-s. Kim, C. Kim, O.-H. Rho, S.K. Hong, Cures for the shock instability: development of a shock-stable roe scheme, J. Comput. Phys. 185 (2) (2003) 342–374.
[16] S.D. Kim, B.J. Lee, H.J. Lee, I.-S. Jeung, Robust HLLC Riemann solver with weighted average flux scheme for strong shock, J. Comput. Phys. 228 (20) (2009) 7634–7642.
[17] S.D. Kim, B.J. Lee, H.J. Lee, I.-S. Jeung, J.-Y. Choi, Realization of contact resolving approximate Riemann solvers for strong shock and expansion flows, Int. J. Numer. Methods Fluids 62 (10) (2010) 1107–1133.

[18] A. Harten, P.D. Lax, B. Van Leer, On upstream differencing and Godunov-type scheme for hyperbolic conservation laws, SIAM Rev. 25 (1) (1983) 35–61.
[19] E.F. Toro, M. Spruce, W. Speares, Restoration of the contact surface in the HLL-Riemann solver, Shock Waves 4 (1) (1994) 25–34.
[20] B. Srinivasan, A. Jameson, S. Krishnamoorthy, An upwinded state approximate Riemann solver, Int. J. Numer. Methods Fluids 70 (5) (2012) 578–602.
[21] M.-S. Liou, A sequel to AUSM: AUSM+, J. Comput. Phys. 129 (2) (1996) 364–382.
[22] K. Xu, Z. Li, Dissipative mechanism in Godunov-type schemes, Int. J. Numer. Methods Fluids 37 (1) (2001) 1–22.
[23] M. Dumbser, J.-M. Moschetta, J. Gressier, A matrix stability analysis of the carbuncle phenomenon, J. Comput. Phys. 197 (2) (2004) 647–670.
[24] Y. Chauvat, J.-M. Moschetta, J. Gressier, Shock wave numerical structure and the carbuncle phenomenon, Int. J. Numer. Methods Fluids 47 (8–9) (2005) 903–909.
[25] K. Kitamura, P. Roe, F. Ismail, Evaluation of Euler fluxes for hypersonic flow computations, AIAA J. 47 (1) (2009) 44–53.
[26] D. Zaide, P. Roe, Shock capturing anomalies and the jump conditions in one dimension, in: 20th AIAA Computational Fluid Dynamics Conference, 2011, p. 3686.
[27] K. Kitamura, E. Shima, Towards shock-stable and accurate hypersonic heating computations: a new pressure flux for AUSM-family schemes, J. Comput. Phys. 245 (2013) 62–83.
[28] K. Xu, Gas Evolution Dynamics in Godunov-type Schemes and Analysis of Numerical Shock Instability, Institute for Computer Applications in Science and Engineering (ICASE), 1999.
[29] B. Einfeldt, On Godunov-type methods for gas dynamics, SIAM J. Numer. Anal. 25 (2) (1988) 294–318.
[30] P. Roe, Approximate Riemann solvers, parameter vectors, and difference schemes, J. Comput. Phys. 135 (2) (1997) 250–258.
[31] S. Osher, F. Solomon, Upwind difference schemes for hyperbolic systems of conservation laws, Math. Comput. 38 (158) (1982) 339–374.
[32] M. Dumbser, D.S. Balsara, A new efficient formulation of the HLLEM Riemann solver for general conservative and non-conservative hyperbolic systems, J. Comput. Phys. 304 (2016) 275–319.
[33] S.H. Park, J.H. Kwon, On the dissipation mechanism of Godunov-type schemes, J. Comput. Phys. 188 (2) (2003) 524–542.
[34] F. Ismail, P.L. Roe, Affordable, entropy-consistent Euler flux functions, ii: entropy production at shocks, J. Comput. Phys. 228 (15) (2009) 5410–5436.
[35] A. Harten, High resolution schemes for hyperbolic conservation laws, J. Comput. Phys. 135 (2) (1997) 260–278.
[36] A. Harten, J.M. Hyman, Self adjusting grid methods for one-dimensional hyperbolic conservation laws, J. Comput. Phys. 50 (2) (1983) 235–269.
[37] V.V. Rusanov, The calculation of the interaction of non-stationary shock waves and obstacles, USSR Comput. Math. Math. Phys. 1 (2) (1962) 304–320.
[38] J.L. Steger, R. Warming, Flux vector splitting of the inviscid gasdynamic equations with application to finite-difference methods, J. Comput. Phys. 40 (2) (1981) 263–293.
[39] F. Ismail, Toward a Reliable Prediction of Shocks in Hypersonic Flow: Resolving Carbuncles with Entropy and Vorticity Control, Ph.D. thesis, University of Michigan, 2006.
[40] S.K. Godunov, A difference method for numerical calculation of discontinuous solutions of the equations of hydrodynamics, Mat. Sb. 89 (3) (1959) 271–306.
[41] M.-S. Liou, A sequel to AUSM, part ii: AUSM+-up for all speeds, J. Comput. Phys. 214 (1) (2006) 137–170.
[42] K.H. Kim, C. Kim, O.-H. Rho, Methods for the accurate computations of hypersonic flows, I: AUSMPW+ scheme, J. Comput. Phys. 174 (1) (2001) 38–80.
[43] E. Shima, K. Kitamura, Parameter-free simple low-dissipation AUSM-family scheme for all speeds, AIAA J. 49 (8) (2011) 1693–1709.
[44] J. Edwards, Towards unified CFD simulations of real fluid flows, in: 15th AIAA Computational Fluid Dynamics Conference, 2001, p. 2524.
[45] H. Nishikawa, K. Kitamura, Very simple, carbuncle-free, boundary-layer-resolving, rotated-hybrid Riemann solvers, J. Comput. Phys. 227 (4) (2008) 2560–2581.
[46] S. Henderson, J. Menart, Grid study on blunt bodies with the carbuncle phenomenon, in: 39th AIAA Thermophysics Conference, 2007, p. 3904.
[47] P. Woodward, P. Colella, The numerical simulation of two-dimensional fluid flow with strong shocks, J. Comput. Phys. 54 (1) (1984) 115–173.